



HAL
open science

Geochemical systematics of Pb isotopes, fluorine, and sulfur in melt inclusions from São Miguel, Azores

Estelle F. Rose-Koga, K.T. Koga, M. Moreira, Ivan Vlastélic, M.G. Jackson, M.J. Whitehouse, N. Shimizu, N. Habib

► To cite this version:

Estelle F. Rose-Koga, K.T. Koga, M. Moreira, Ivan Vlastélic, M.G. Jackson, et al.. Geochemical systematics of Pb isotopes, fluorine, and sulfur in melt inclusions from São Miguel, Azores. *Chemical Geology*, 2017, 458, pp.22 - 37. 10.1016/j.chemgeo.2017.03.024 . hal-01636195

HAL Id: hal-01636195

<https://uca.hal.science/hal-01636195>

Submitted on 26 Nov 2020

HAL is a multi-disciplinary open access archive for the deposit and dissemination of scientific research documents, whether they are published or not. The documents may come from teaching and research institutions in France or abroad, or from public or private research centers.

L'archive ouverte pluridisciplinaire **HAL**, est destinée au dépôt et à la diffusion de documents scientifiques de niveau recherche, publiés ou non, émanant des établissements d'enseignement et de recherche français ou étrangers, des laboratoires publics ou privés.

Geochemical systematics of Pb isotopes, fluorine, and sulfur in melt inclusions from São Miguel, Azores

EF Rose-Koga¹, KT Koga¹, M Moreira², I Vlastelic¹, MG Jackson³, MJ Whitehouse⁴, N Shimizu⁵, N Habib⁶

(1) Laboratoire Magmas et Volcans, Université Blaise Pascal - CNRS - IRD, OPGC, 6 Avenue Blaise Pascal, 63178 Aubière, France

(2) Laboratoire de Géochimie et Cosmochimie, Institut de Physique du Globe de Paris, Sorbonne Paris Cité, Univ. Paris Diderot, UMR 7154 CNRS, 1 rue Jussieu, 75238 Paris, France

(3) University of California Santa Barbara, Department of Earth Science, Santa Barbara, CA, 93109-9630, USA

(4) Swedish Museum of Natural History, Box 50 007, SE-104 05 Stockholm, Sweden

(5) Woods Hole Oceanographic Institution, Dpt Geology & Geophysics, MA, USA

(6) UFR LACC, Université Blaise Pascal, Clermont-Ferrand, France

Abstract

Pb isotopic measurements in olivine-hosted melt inclusions of ocean island basalts (OIBs) from São Miguel, Azores, reflect the high $^{207}\text{Pb}/^{204}\text{Pb}$ and $^{208}\text{Pb}/^{204}\text{Pb}$ at a given $^{206}\text{Pb}/^{204}\text{Pb}$ of their host lavas. The data are consistent with a mixture between two endmembers: the first (the Central Group) has relatively high $^{208}\text{Pb}/^{206}\text{Pb}$ and is similar to the component sampled by Graciosa and Faial, and the second is a radiogenic endmember (with low $^{208}\text{Pb}/^{206}\text{Pb}$) that we refer to as the Nordeste component. F and Cl concentrations measured in the same melt inclusions from São Miguel represent parental abundances unmodified by crustal assimilation. Based on undegassed F and Cl concentrations, the source beneath São Miguel is volatile-rich. Among melt inclusions, Pb-isotope compositions correlate positively with S concentrations: we attribute this correlation to the dissolution of oceanic crust sulfides in the S-undersaturated basaltic melt of the Nordeste component. The blebs were assimilated by São Miguel magma and the magma droplets were later trapped in olivines.

When comparing melt inclusions from worldwide OIBs representing mantle endmembers, we find a global negative correlation between F/Nd and $^{208}\text{Pb}/^{206}\text{Pb}$ of volcanic glasses and melt inclusions. The high F/Nd (up to 40) endmember is represented by HIMU melt inclusions and the low F/Nd (down to 14) by EM1 Pitcairn glasses. São Miguel melt inclusions have an intermediate F/Nd = 23.1 ± 3.4 .

Keywords: melt inclusions, Pb isotopes, F/Nd, halogen, volatile elements, São Miguel

1. Introduction

The Azores archipelago comprises nine hotspot-related volcanic islands in the northern Atlantic, and a mantle plume has been resolved under the islands (French and Romanowicz, 2015). The geochemistry of Azores lavas is well documented (e.g. White et al., 1979; Schilling et al., 1980; Widom and Shirey, 1996; Turner et al., 1997; Moreira et al., 1999; 2012; Widom, 2002; Widom and Farhquar, 2003; Beier et al., 2007; Elliott et al., 2007).

43 Previous studies have used helium isotopes to identify three groups of islands in the Azores:
44 the “Central Group” (with Terceira, Pico, and São Jorge) has the most “primitive” helium
45 signature (i.e. low $^4\text{He}/^3\text{He}$, down to 39,200; R/Ra=18.4), the eastern group has radiogenic
46 helium (with São Miguel, $^4\text{He}/^3\text{He} > 140,000$; R/Ra < 5.1), and the western group has a mid
47 ocean ridge basalt--like (MORB)helium signature (i.e. $^4\text{He}/^3\text{He}$ around $88,000 \pm 5000$;
48 R/Ra=8; e.g. Moreira et al., 1999; 2012). Additionally, halogen concentrations are
49 latitudinally graded from 30 to 50°N, crossing the Azores and the Mid-Atlantic Ridge
50 (MAR), and a Cl-, Br-, and F-rich component was identified beneath the Central Group and
51 the nearby ridge (Schilling et al., 1980). Recently, a water-rich mantle domain was proposed
52 as the source of lavas from Pico (Métrich et al., 2014).

53 São Miguel is the largest and easternmost island of the Azores. Additionally, São Miguel is
54 possibly one of the oldest islands in the archipelago (up to 4 Ma; Abdel-Monem et al., 1975;
55 Moore, 1990), although this age of 4 Ma is debated (Johnson et al., 1998). Based on trace
56 element concentrations and stable and radiogenic isotopic compositions, there is now a
57 consensus among geochemists that the lavas from São Miguel represent a mixture between
58 two endmembers: one with a HIMU-like Pb isotope composition (also found in São Jorge;
59 Millet et al., 2009) and the second with a less radiogenic Pb isotopic composition common to
60 the other islands of the Central Group (Widom and Shirey, 1996; Turner et al., 1997; Widom,
61 2002; Widom and Farhquar, 2003; Beier et al., 2007). The HIMU-like endmember has been
62 argued to result from underplated basalt intruded into oceanic lithospheric mantle (Elliott et
63 al., 2007) or from recycled material such as oceanic crust to which a small amount of evolved
64 melt is added (<5%; Beier et al., 2007). A recent study combining helium and neon isotopes
65 presented strong evidence for a recycled mafic magma as the origin of the HIMU component
66 in the Azores (Moreira et al., 2012), corroborating the two previous studies.

67 However, with the exception of He and Ne, little data are reported for the volatile element
68 characteristics of the São Miguel lavas (Moreira et al., 1999; 2012). Our study investigates
69 the presence (or absence) of a Cl- and F-rich component in the mantle source under São
70 Miguel, which would complement the existence of such a component beneath the Central
71 Group (Schilling et al., 1980). We report new volatile element concentrations and Pb-isotopic
72 data in olivine-hosted melt inclusions from São Miguel lavas. We identify a correlation
73 between Pb-isotopes and S concentrations in the melt inclusions, and we attribute this
74 correlation to the dissolution of sulfides (most likely of crustal origin) in a S-undersaturated

75 basaltic melt. Thus, this correlation demonstrates the role of sulfide in controlling the Pb-
76 isotope composition in São Miguel inclusions. The volatile characteristics (Cl/K₂O and F/Nd)
77 of the São Miguel parental magma are compared to hotspot mantle endmembers such as
78 HIMU (Mangaia), enriched mantle I (EMI, Pitcairn), and enriched mantle II (EMII, Samoa).
79 We show that olivine-hosted melt inclusions and submarine volcanic glasses from OIBs
80 representing mantle endmembers have F/Nd that correlates with Pb-isotopes, and shows high
81 F/Nd in the source of HIMU lavas and low F/Nd in the source of EMI and MORB lavas.
82

83 **2. Sample description**

84 The Azores Plateau is situated in the vicinity of the triple junction formed by the MAR and
85 the ultraslow Terceira spreading axis (2–4 mm/a; Vogt and Jung, 2004). São Miguel, located
86 125 km west of the easternmost island, is host to five volcanic systems (from west to east):
87 Sete Cidades, Picos, Fogo, Furnas, and Nordeste (Fig. 1). The oldest subaerial eruption unit is
88 at the base of Sete Cidades. The Fogo (~200 ka) and Nordeste lavas (780–880 ka) are found
89 below Furnas, which has lavas as old as 93 ka (Johnson et al. 1998). In this study, we
90 examine olivine-hosted melt inclusions from six lavas of São Miguel. Whole rock sample
91 descriptions have been provided in previous studies (Moreira et al., 1999; 2012): one sample
92 (ACO95-03) is from the 1563 historical Queimado peak basanitoid lava flow in the Fogo
93 volcanic system, four samples (ACO95-62; ACO95-68; 2000-4; 2000-9) are Nordeste
94 ankaramites, and the sixth sample (ACO95-56) is from the Picos volcanic system.

95 **3. Methods**

96 *3.1 Melt inclusion homogenization procedure*

97 Helium isotope compositions of olivine phenocrysts from these six samples have been
98 documented, and a subset analyzed for neon isotopes (Moreira et al. 1999; 2012). From these
99 six rocks, we measured 19 olivine-hosted melt inclusions for Pb isotopes and volatile element
100 concentrations (F, S, and Cl), and H₂O and CO₂ were measured on 9 of these inclusions. All
101 melt inclusions were crystalline and required homogenization to generate glassy textures for
102 analysis. Details of sample preparation procedures, including homogenization methods, are
103 described elsewhere (Le Voyer et al., 2008, 2010). In brief, homogenization was performed
104 on a Vernadsky-type heating stage. In order to both avoid oxidation of the host mineral and
105 improve the quench rate, the oxygen fugacity was kept between 10⁻¹⁰ and 10⁻⁹ atm using He

106 that is purified with Zr at 700°C. The melt inclusions were heated until the last daughter
107 mineral disappeared, kept at this “homogenization temperature” for 5 additional minutes, and
108 then quenched. The homogenization procedure lasted 25 minutes total and the
109 homogenization temperature was 1200±15°C (see Le Voyer et al., 2008, 2010 for details on
110 the homogenization procedure, and a volatile loss assessment in the supporting material of
111 Cabral et al., 2014). Olivines spent less than 5 minutes above 1200°C in the heating stage,
112 preventing any significant H₂O loss from the melt inclusion, as shown in a prior study using
113 the same heating stage at Clermont-Ferrand (Chen et al., 2011). Melt inclusions were
114 exposed and polished individually, first on silicon carbide then with diamond paste of
115 decreasing granular sizes (6, 3, and 1 μm). All polished inclusion-bearing olivines were
116 pressed into a one-inch high-purity indium mount and polished with a ¼ μm alumina paste
117 for 5 min to remove all scratches from the exposed surface of the glassy melt inclusions. The
118 mount was then washed in an ultrasonic bath of pure ethanol for 10 min and then in distilled
119 water for 10 min. The mount was dried in an oven at 100°C for at least 24 hours before final
120 gold-coating. Prior to analysis, the mount was placed for at least 12 hours under high vacuum
121 (~10⁻⁸ Torr) to reduce surface adsorption of volatile elements.

122

123 *3.2 Standards and calibration for SIMS Pb-isotope measurements*

124 The Pb isotope ratios were measured by secondary ion mass spectrometry (SIMS) on the
125 multicollection SIMS 1280 located at the National Museum of Natural History (NMNH) in
126 Stockholm, Sweden.

127 Repeat ²⁰⁷Pb/²⁰⁶Pb measurements of GOR132 glass standard (19 ppm Pb; Jochum et al., 2006)
128 and R124 (homogeneous Reunion island glass; 2 ppm Pb) yielded errors of 0.40% and 0.96%
129 (2 sigma), respectively (95% confidence interval; Fig. 4). A brief summary of the ion probe
130 settings for Pb isotopic analysis follows. Prior to analysis, a 90 second pre-sputter with a 25 x
131 25 μm raster cleaned the surface of the sample. After the pre-sputter, the raster was stopped
132 for analyses. During analysis, a focused O²⁺ primary beam of 8 nA sputtered the sample, with
133 a primary accelerating voltage of 13 kV. We used a Kohler illumination method that resulted
134 in a 15 μm flat-bottomed pit centered in the 25 μm square raster-cleaned area. Secondary
135 positive ions were accelerated at 10 kV and analyzed at mass resolution of 4800 to avoid any
136 mass interference. The size of the field aperture was set at 4000 μm, and the contrast aperture

137 at 400 μm . The centered energy window was adjusted to ± 45 eV. The multicollection system
138 was composed of 5 ion-counting electron multipliers set on moveable trolleys (L2, L1, C, H1
139 and H2). The detection array was configured to measure $^{204}\text{Pb}^+$ in the electron multiplier set
140 on the trolley position L2, $^{206}\text{Pb}^+$ in L1, $^{207}\text{Pb}^+$ in C (placed on the ion optical axis) and $^{208}\text{Pb}^+$
141 in H1. The measurements were conducted over 40 to 120 cycles with a 20 s counting time for
142 each mass and a deadtime correction of 60 ns. A measurement lasted approximately 20 min
143 for 40 cycles. With this setting, the sensitivity on ^{208}Pb is 19 cps/ppm/nA (e.g. Rose-Koga et
144 al., 2012; Rose-Koga et al., 2014).

145 A detailed description and discussion regarding Pb isotope measurements by
146 multicollection SIMS is found in the supporting material of a previous study (Rose-Koga et
147 al., 2012), where we analyzed the Pb-isotopic compositions of several standards with a wide
148 range of SiO_2 concentrations (46 to 76 wt. %). The set of standards analyzed have dissimilar
149 matrices, and the measured Pb isotope compositions did not suggest a matrix dependent mass
150 fractionation. The trend formed by the standard data in Pb isotope space has a slope that is
151 generally consistent with mass dependent fractionation (for details see Rose-Koga et al.,
152 2012; supp. Material).

153 *3.3 Volatile, major, and trace element analysis*

154 Volatile element concentrations (H_2O , CO_2 , F, S, and Cl) were measured by monocollection
155 SIMS on the Cameca 1280 at WHOI (Woods Hole Oceanographic Institution, USA) on 11
156 melt inclusions. F, S, and Cl were measured by Electron Micro Probe (EMP) at LMV
157 (Laboratoire Magmas et Volcans, France) on the remaining melt inclusions. The mono-
158 collection SIMS settings employed here are standard and described elsewhere (Rose-Koga et
159 al., 2008; Supplementary Table S5 in Helo et al., 2011; Rose-Koga et al., 2012). In short, we
160 used a Cs^+ primary beam with a current of 1.5 nA and an electron gun to compensate for
161 charge build-up at the sample surface. After a 3 minute pre-sputtering with 30 x 30 μm
162 square raster, analyses were performed on the central 15 μm spot centered in the rastered area
163 by a mechanical aperture placed at the secondary ion image plane. The mass resolving power
164 of 6600 allowed complete discrimination of interferences ($^{34}\text{S}^1\text{H}$ on ^{35}Cl , ^{17}O on $^{16}\text{O}^1\text{H}$, $^{29}\text{Si}^1\text{H}$
165 on ^{30}Si and $^{31}\text{P}^1\text{H}$ on ^{32}S). We used a critical illumination method, a 400 μm contrast aperture
166 and a ± 30 eV energy slit opening. Each measurement lasted approximately 15 minutes. The
167 maximum uncertainties on the ion probe dataset, taking into account the reproducibility over

168 10 cycles of analyses and the uncertainties on the regression of the calibration line, were less
169 than 5% for H₂O, 15% for CO₂, and 10% for Cl, F, and S (1 σ).

170 Major elements were measured by EMP (Cameca SX 100 at LMV, France) in all melt
171 inclusions, using standard procedures outlined in Le Voyer et al. (2008). F, S, and Cl were
172 also measured by EMP at LMV on 9 melt inclusions. Cl, S, and F analyses were performed at
173 80 nA and with a 5 to 20 μ m defocused beam together with the trace element acquisition
174 program proposed in the Cameca Peak Sight software. The analytical standards were: natural
175 scapolite for the Cl $K\alpha$ line, fluorite for F $K\alpha$, and VG-2 glass for S $K\alpha$. The sulfur
176 concentration in VG-2 glass is assumed to be 1340 ppm; this value corresponds to the
177 average of a compilation of published data (Dixon *et al.* 1991; Thordarson *et al.* 1996).
178 Chlorine and sulfur were analyzed successively by using a large pentaerythritol (LPET)
179 crystal and F was analyzed using a thallium acid phtalate (TAP) diffraction crystal. With 15
180 kV accelerating voltage and 80 nA beam current, counting time of 100 sec (Cl and S) and
181 600 sec (F), detection limits for S, Cl, and F were \sim 35, 50, and 200 ppm, respectively. The
182 total analytical error for S, Cl, and F including precision and accuracy of measurements, was
183 20% (relative uncertainty) for S and 30% for Cl and F over the range of concentrations in our
184 inclusions (Rose-Koga et al., 2008). Repeat analyses of standard VG-2 for F, S, and Cl gave
185 values of 597 \pm 49, 130 \pm 11, and 210 \pm 10 ppm (\pm 1 σ), respectively.

186 Trace element measurements were carried out at LMV using a laser ablation system (193 nm
187 Excimer Resonetics M-50E) coupled with an Agilent 7500 cs inductively coupled plasma
188 mass spectrometer (LA-ICPMS). A laser spot size of 33 microns was used. Analyses were
189 made with a laser pulse frequency of 2 Hz with a maximum output energy of 6 mJ. Twenty
190 masses were collected with an integration time of 20 ms per mass: ⁸⁵Rb, ⁸⁸Sr, ⁸⁹Y, ⁹⁰Zr, ⁹³Nb,
191 ¹³⁷Ba, ¹³⁹La, ¹⁴⁰Ce, ¹⁴³Nd, ¹⁴⁵Nd, ¹⁴⁶Nd, ¹⁴⁷Sm, ¹⁵³Eu, ¹⁵⁷Gd, ¹⁶³Dy, ¹⁶⁶Er, ¹⁷⁸Hf, ²⁰⁴Ta, ²³²Th, and
192 ²³⁸U. The internal reference mass was ⁴⁴Ca, where the CaO concentrations were measured by
193 electron microprobe. A typical signal acquisition started by collecting a background signal
194 for 30 seconds followed by a laser firing for 70 seconds or less, depending on the thickness of
195 the melt inclusion. NIST 610 glass was used as an external standard. NIST 612 and BCR-2G
196 glasses (Gao et al, 2007) were also analyzed to check the accuracy and precision of the
197 analyses. Relative 1 σ standard errors are better than 3% for Rb, Sr, Y, Zr, Nb, Ba, La, and
198 Ce, less than 4% for Nd, better than 9% for Sm, Eu, Gd, Dy, Er, Hf, Ta, Th, and U, and 12%
199 for Yb.

200

201

202 **4. Results**

203 Volatile element abundances and Pb isotope compositions are reported in Table 1 and major
204 element concentrations in Table 2. Trace element abundances are reported in Table 3.

205 *4.1. Major and trace element compositions*

206 The forsterite contents (mol %) of the host olivines range from 77 to 89. Within each olivine
207 grain, there are less than 0.7% relative variations of major element concentrations based on 2
208 to 3 electron microprobe analyses of each grain, indicating a lack of significant intra-grain
209 compositional heterogeneity. Crystallization of olivine from the wall of the melt inclusion
210 after entrapment changes the major and trace element composition of the melt inclusion. This
211 is a reversible process that is corrected for during the homogenization procedure and
212 correction for post-entrapment olivine overgrowth (also called Post Entrapment
213 Crystallization, PEC). This correction dissolves (or crystallizes) increments of equilibrium
214 olivine into the melt inclusion liquid until the Fe-Mg K_D reaches the equilibrium value (0.3;
215 Toplis, 2005). The mass fractions of olivine added to the inclusions in this correction
216 procedure were less than 13% of the melt for all but 2 inclusions, which required 16 and 20%
217 olivine correction (9/1/00 and ACO95-56a, respectively; Suppl. Material). SiO_2
218 concentrations of the corrected melt compositions range from 42 to 53 wt. %. The olivine
219 correction contributes negligible changes to the SiO_2 concentrations, as the range in SiO_2
220 before correction was 42 to 52 wt. % and the melt inclusions with extreme SiO_2
221 concentrations before correction remain the extreme ones after correction. The correction
222 mostly affects MgO concentrations of the melt inclusions: MgO before correction varies from
223 6.42 to 17.2 wt. %, and after correction between 3.17 and 15.5 wt. %. In a plot of total alkali
224 versus SiO_2 , the melt inclusion corrected compositions fall in the fields of tephrite basanite,
225 basalt, trachy-basalt, and basaltic trachy-andesite. These compositions overlap with the whole
226 rock compositions of the mafic magmatic series of São Miguel (Fig. 2).

227 Compared to a typical MORB, trace element abundances in the melt inclusions show a light
228 rare earth element (LREE) enriched pattern (Fig. 3a). Separate melt inclusions plot
229 essentially parallel to each other in the spidergram. REE patterns of Pico melt inclusions
230 overlap with those of São Miguel melt inclusions (Fig. 3a). By plotting all analyzed lithophile

231 trace elements in an approximate compatibility order for MORB, significant enrichment of
232 the most incompatible elements (e.g., Rb, Ba, Th, U and Nb) is also apparent (Fig. 3b). The
233 São Miguel melt inclusions have average Ba/La = 10.0 ± 1.1 , 11% relative standard deviation.
234 The Ba/La for São Miguel whole rocks (Georoc database filtered for mafic lavas: $42 < \text{SiO}_2 <$
235 53 wt. %) is statistically the same (10.9 ± 1.8), attesting to the similarity between the
236 spidergram patterns of whole rocks and melt inclusions. Similarly, the ratio of an
237 incompatible element and a moderately incompatible element, Sr/Yb, gives values of 278 ± 88
238 and 325 ± 88 for the São Miguel whole rocks and melt inclusions, respectively.

239 *4.2. Pb isotope compositions*

240 In Pb isotope space, São Miguel (i.e., Nordeste component) whole rocks display a different
241 trend compared to the Central Group ($^{206}\text{Pb}/^{204}\text{Pb}$ vs $^{208}\text{Pb}/^{204}\text{Pb}$; Fig. 5 insert), and the rocks
242 from which we picked the olivines in this study represent extreme compositions of the
243 Nordeste component: they come from samples with among the highest $^{208}\text{Pb}/^{204}\text{Pb}$ from São
244 Miguel (between 40.05 and 40.45, inset of Fig. 5; ACO95-03, -56, -62, and -68). The trend of
245 melt inclusions extends towards lower $^{207}\text{Pb}/^{206}\text{Pb}$ values than those reported in the literature
246 for the whole rocks. However, it should be cautioned that the size of external
247 reproducibilities of standards is comparable to the range of Pb isotope variability in melt
248 inclusions observed in samples ACO95-68 and ACO95-03, suggesting that the isotopic
249 heterogeneity found within these rocks are statistically insignificant (Fig. 4). The $^{208}\text{Pb}/^{206}\text{Pb}$
250 and $^{207}\text{Pb}/^{206}\text{Pb}$ variability found in samples ACO95-56 and ACO95-62, on the other hand,
251 exceeds analytical uncertainty (2σ). Sample ACO95-62 shows $^{208}\text{Pb}/^{206}\text{Pb}$ variations at nearly
252 constant $^{207}\text{Pb}/^{206}\text{Pb}$, whereas $^{208}\text{Pb}/^{206}\text{Pb}$ and $^{207}\text{Pb}/^{206}\text{Pb}$ variations are positively correlated in
253 sample ACO95-56. Nevertheless, we stress that the general trend formed by the melt
254 inclusions in a $^{207}\text{Pb}/^{206}\text{Pb}$ versus $^{208}\text{Pb}/^{206}\text{Pb}$ diagram (Fig. 5) is in good agreement with
255 previous São Miguel literature data for whole rock lavas (e.g. Davies et al., 1989; Turner et
256 al., 1997; Widom et al., 1997; Moreira et al., 1999; Elliott et al., 2007; Beier et al., 2007).
257 ^{204}Pb normalized ratios vary within the analytical uncertainty of the measurements, and in
258 $^{208}\text{Pb}/^{204}\text{Pb}$ vs $^{206}\text{Pb}/^{204}\text{Pb}$ isotopic space, the variation of the whole rock data plot along a ^{204}Pb
259 error line (not shown). Therefore, it is not possible to identify statistically significant isotopic
260 variation among the São Miguel melt inclusion samples in ^{204}Pb normalized isotope space,
261 and ^{204}Pb normalized data are not shown in the figure.

262 *4.3. Volatile element concentrations*

263 H₂O and CO₂ concentrations in the São Miguel melt inclusions are lower than those reported
264 for primitive melt inclusions from oceanic lavas at other localities. In recent melt inclusion
265 studies, H₂O and CO₂ contents are routinely corrected for the fluid-phase bubble that is
266 present in melt inclusions (e.g. Shaw et al., 2008, 2010; Koleszar et al., 2009). However, the
267 volatile element concentrations are not corrected in this study, because the size of the bubble
268 (when present) was not systematically measured prior to polishing the melt inclusions. The
269 data display a large range of H₂O concentrations (from 107 to 1552 ppm) that are lower than
270 those in melt inclusions from neighbouring Pico island (4000 to 21000 ppm; Métrich et al.,
271 2014). Indeed, from the perspective of oceanic hotspot lavas, the São Miguel melt inclusions
272 reported here have low H₂O concentrations. São Miguel melt inclusions average 900ppm
273 H₂O, up to 12 times lower than some MORB glasses (between 1000 and 5200 ppm; e.g.
274 Shimizu unpublished Famous MI data, Shaw et al., 2010; 800-11000 ppm; Le Voyer et al.,
275 2015; Shimizu et al., 2016).

276 Relatively low CO₂ concentrations, ranging from 77 to 1178 ppm, accompany the low H₂O
277 contents of São Miguel melt inclusions. The CO₂ abundances are in the lower range of that
278 reported for the melt inclusions of Pico Island (697 to 4039 ppm), but are similar to the range
279 of CO₂ in Mid Atlantic Ridge Lucky Strike melt inclusions (153 to 1498 ppm; Wanless et al.,
280 2015).

281 Chlorine abundances in our melt inclusions are between 335±7 to 966±43 ppm (Fig. 6), and
282 are comparable to Pico melt inclusions (330 to 900 ppm; Métrich et al., 2014; Fig. 6). Unlike
283 many melt inclusions from oceanic lavas, Cl does not correlate with K₂O or other trace
284 elements (e.g., Nb) that are similarly incompatible.

285 F concentrations in the melt inclusions vary from 637±98 to 1399±10 ppm (Fig. 6),
286 comparable to the melt inclusions from Pico Island (742 to 1442 ppm; Métrich et al., 2014). F
287 and K₂O concentrations correlate positively. The F/K₂O ratios of São Miguel melt inclusions
288 are identical to those of Pico melt inclusions (336 and 332, respectively). These values are
289 higher than Atlantic MORB glasses (71 to 519 ppm; Le Voyer et al., 2015). The F
290 concentrations in Azores melt inclusions resemble those of Samoan submarine glasses (818
291 to 1887 ppm; Workman et al., 2006), and the range extends to higher values than in olivine-
292 hosted melt inclusions from hotspot basalts such as the Yellowstone hot spot (55 to 977 ppm;

293 Stefano et al., 2011). Extreme HIMU melt inclusions from Mangaia have generally higher F
294 concentrations (1180 to 1950 ppm; Cabral et al., 2014; Fig. 6).

295 S concentrations in São Miguel melt inclusions are between 311 ± 34 and 2115 ± 56 ppm
296 (Table 1). Sulfur is usually considered to be incompatible in silicate minerals, but shows no
297 consistent trend with other incompatible elements in São Miguel melt inclusions. S
298 concentrations in São Miguel melt inclusions decrease with decreasing FeO concentration.
299 The range of S concentrations in São Miguel melt inclusions overlaps with that of melt
300 inclusions from Pico Island (1195 to 1954 ppm; Métrich et al., 2014). São Miguel melt
301 inclusions are sulfide saturated (see Discussion, below); for comparison, Pico melt inclusions
302 are also described as sulfide saturated (Métrich et al., 2014).

303

304 **5. Discussion**

305 *5.1. Assessment of parental magma compositions from São Miguel melt inclusions*

306 The olivine-hosted melt inclusions in this study represent parental magmas of the São Miguel
307 lavas. First, host-olivines found in basaltic lavas are generally forsteritic (77 to 89, with an
308 average of 84). Second, trace element patterns (Fig. 3a) lack pronounced Sr and Eu
309 anomalies, and the small negative anomalies in Ba and Sr do not correlate with Al_2O_3 , Na_2O ,
310 or CaO, indicating only minor (if any) plagioclase fractionation, and suggesting no crustal
311 assimilation took place (Fig. 3a). Significant plagioclase fractionation or assimilation in the
312 underlying oceanic crust is therefore unlikely. Because of the forsteritic host-olivine
313 compositions and the lack of significant crustal modification, we conclude that these melt
314 inclusions were trapped at an early stage of crystallization from a little-modified, mantle-
315 derived primitive magma.

316 Compositional corrections for post-entrapment crystallization and degassing of melt
317 inclusions are viable only for inclusions that did not experience diffusive exchange with the
318 magma surrounding the host olivine. In reality, the host olivine can continuously exchange Fe
319 and Mg with the surrounding magma, potentially leading to Fe-loss from melt inclusions.
320 Therefore, exact reconstruction of the FeO and MgO content of the parental magma cannot
321 be achieved (Danyushevsky et al., 2000; 2002; Gaetani and Watson, 2000). However, the
322 ratios of incompatible trace elements remain unmodified as they are not partitioned into
323 olivine, and are therefore representative of the primitive parental magma. Note that the trace

324 element and REE patterns of the São Miguel melt inclusions are roughly parallel and tightly
325 distributed (Fig. 3a,b), and Ba/La and Sr/Yb ratios of whole rocks and melt inclusions are
326 statistically indistinguishable.

327 The REE patterns of São Miguel and Pico melt inclusions overlap (Fig. 3a). Since Sr and Yb
328 have different compatibilities during mantle melting, the lack of variation of Sr/Yb ratios in
329 both São Miguel (286 ± 87) and Pico (244 ± 43) melt inclusions indicates that the primitive
330 magmas of the islands are derived from comparable degrees of partial melting of a similar
331 initial lithology. Furthermore, the lack of variation of Ba/La (10 ± 1 for São Miguel and 9 ± 1
332 for Pico), a ratio of two highly incompatible elements, indicates that the magmas were
333 derived from a similar initial bulk lithology.

334 Here, the term “initial lithology” represents the material prior to melting. It is used to
335 distinguish from the term “magma source”. The latter refers to isotopically distinct entities
336 that are involved in the magma genesis (in particular, Pb isotopes in this study). Thus, the
337 trace element similarity between Pico and Saõ Miguel whole rocks suggest the presence of a
338 single dominant initial lithology with similar bulk chemistry (e.g. White et al., 1979; Turner
339 et al., 1997; Elliott et al., 2007; Beier et al., 2007). However, there exist distinct magma
340 sources that contribute to the observed isotopic variations (e.g. Davies et al., 1989; Kurz,
341 1993; Turner et al., 1997; Moreira et al., 1999; Widom et al., 1996, 1997, 2003).

342 It should be noted that these melt inclusion samples are hosted in whole rocks that span a
343 range of ages (300 ky to present) and geographical locations (55 km east-west on São
344 Miguel). The similarity of trace element characteristics among São Miguel whole rock basalts
345 has been noted in previous studies (White et al., 1979; Elliott et al., 2007; Beier et al., 2007),
346 and the melt inclusion trace element data presented here corroborate earlier observations. The
347 similarity of parental magmas can be extended geographically to other volcanoes on different
348 islands of the Azores archipelago. Several previous whole rock studies noted nearly identical
349 trace element characteristics among Faial, Pico, and São Jorge (White et al., 1979; Turner et
350 al., 1997; Beier et al., 2007, 2012). It appears that, based on major and trace element
351 compositions of basalts and melt inclusions, the mantle beneath these Azores islands must
352 have a similar lithology to generate such similar trace element patterns, with geodynamic
353 conditions permitting the production of uniform degrees of partial melting.

354 5.2. Volatile element characteristics of São Miguel melt inclusions

355 5.2.1. “Lost” volatiles: H₂O and CO₂

356 The parental magma beneath São Miguel records the lowest degree of partial melting in the
357 archipelago (<4%; Bourdon et al., 2005), allowing the extracted melt to be richer in H₂O
358 compared to typical MORB (0.1–0.5 wt. % H₂O in MORB; Michael, 1988; Dixon and
359 Stolper, 1995; Sobolev and Chaussidon, 1996). Furthermore, a greater H₂O abundance in the
360 initial Azores mantle compared to that of MORB (e.g. 116 ppm Salters and Stracke, 2004)
361 would favor the generation of wet magma. Previous estimates of H₂O abundance in the
362 Azores mantle plume range between 200 ppm (based on melting temperatures and pressures
363 determined by mineral and lava compositions; Beier et al., 2012) and 700 ppm H₂O (based on
364 a pHMELTS model; Asimow et al., 2004). From melt inclusions, an estimate of 680 ppm
365 H₂O is modelled for the mantle beneath Pico Island (Métrich et al., 2014). Using the H₂O
366 content of the mantle beneath Pico Island, and given a degree of partial melting between 2.5
367 and 4% (Bourdon et al., 2005), the H₂O concentration of un-degassed São Miguel melt
368 inclusions could reach values from 1.7 to 2.7 wt. %. In this case, São Miguel melt inclusions
369 have lost up to 91% of their initial H₂O content. Here, the reported H₂O contents of São
370 Miguel melt inclusions represent minimum H₂O values, and do not represent either the initial
371 H₂O concentrations at the time of entrapment or the primitive H₂O abundance of the Azores
372 magma because hydrogen can diffuse from melt inclusions through the host olivine crystal
373 (Chen et al., 2011; Gaetani et al., 2012; Gaetani et al., 2014). An indicator of diffusive
374 hydrogen loss is the correlation of H₂O concentration and melt inclusion size (long or short
375 axis of the melt inclusion, Chen et al., 2011). This correlation is based on the fact that
376 diffusive hydrogen loss is promoted by the larger surface-to-volume ratios of smaller melt
377 inclusions. Among 5 melt inclusions in which H₂O was measured, we found a positive
378 correlation between their sizes (long axis L and short axis l, Table 2) and H₂O contents (R²=
379 0.90 and 0.93, respectively). Melt inclusions from this study have therefore most likely
380 suffered diffusive hydrogen loss through the host olivine. Henceforth, we will consider the
381 measured H₂O concentrations as being affected by H diffusion and representative of
382 minimum H₂O concentrations.

383 Like H₂O, CO₂ measurements represent minimum values. Bubbles are occasionally present in
384 melt inclusions, and such bubbles can contain CO₂. A “bubble correction” might not be
385 significant for H₂O (e.g. <2%; Shaw et al., 2008) but can reach non-trivial values for CO₂

386 (e.g. >80%; Shaw et al., 2008). Therefore, the CO₂ measurements in São Miguel melt
387 inclusions represent minimum values, where most of the CO₂ has potentially degassed to the
388 fluid-phase bubble. Additionally, CO₂ degasses from melt at a greater depth than other
389 volatile elements, and the melt inclusions trapped by olivine at magma chamber depths are
390 likely to have already degassed. This is supported by the observation that CO₂ concentrations
391 correlate poorly with concentrations of refractory incompatible elements (not shown).
392 Therefore the pressure derived from H₂O and CO₂ measurements (using MagmaSat v1.0;
393 Ghiorso, 2015) does not represent the pressure of entrapment (Table 1). The highest
394 entrapment pressure determined for São Miguel melt inclusions is 12MPa and we will use
395 this extremely conservative minimum pressure only for discussion of the potential degassing
396 of other volatile species. Confirmation of the presence or absence of a volatile-rich mantle
397 beneath São Miguel requires constraints from other volatile systems that are less susceptible
398 to diffusive loss from the melt inclusions.

399 5.2.2. Wet São Miguel mantle? Constraints from F and Cl

400 São Miguel melt inclusions are not degassed with respect to F (calculated pressures from
401 Table 1 are higher than the degassing pressure of F, ≈ 10 MPa; Spilliaert et al, 2006). F
402 concentrations correlate positively with K₂O concentration in São Miguel melt inclusions,
403 showing that F is an incompatible element during magma evolution. In fact, F concentrations
404 also generally correlate positively with other incompatible refractory trace elements (e.g. Rb,
405 Sr, Ba, Nb), confirming that F was not lost while H₂O and CO₂ diffused from the melt
406 inclusions.

407 The range of Cl concentrations in melt inclusions from Pico (350 to 900 ppm) and São
408 Miguel (335 to 966 ppm) are identical within uncertainty. Cl can be degassed from erupted
409 lavas, but we argue that Cl was not degassed from the São Miguel melt inclusions prior to
410 entrapment. For example, the degassing pressure threshold for Cl in an H₂O-CO₂-rich alkali
411 basalts of Mount Etna is ~ 100 MPa, and for F ~ 10 MPa (~ 140 MPa for S ; Spilliaert et al.,
412 2006), illustrating the potential for shallow-level Cl degassing and even shallower-level F
413 degassing. However, arc magmas such as Etna are rich in volatile elements, and the pressure
414 thresholds for degassing of Cl and F should be lower for the relatively volatile-poor São
415 Miguel melts.

416 In São Miguel melt inclusions, F and Cl are the two reliable volatile elements for evaluation
417 of primary melt compositions. The SolEx model (Witham et al., 2012) is used to estimate an

418 open-system degassing curve for Cl (F is not feasible with SolEx), assuming the initial
419 undegassed melt contains 2 wt. % H₂O and 5100 ppm CO₂ (Pico melt inclusion compositions
420 from Métrich et al., 2014), 900 ppm Cl and 2100 ppm S (the maxima in this study). Model
421 results show that 99% of the initial Cl remains in the melt during magma ascent. Therefore, at
422 the time of melt entrapment, we consider that most of the magma has not significantly
423 degassed Cl or F.

424 To assess the origin of the undegassed Cl, and decipher if it is characteristic of the source or
425 assimilated materials, we employ the Cl/K₂O ratio as an indicator of assimilation of seawater
426 or seawater-derived materials by mantle melts (e.g. Lassiter et al., 2002). The Cl/K₂O ratio is
427 also easier to compare to other studies since K₂O measurements are readily available in the
428 literature (by comparison, less Cl/Nb data exist). Among OIB melt inclusions, Cl/K₂O in São
429 Miguel melt inclusions, and a few submarine Pitcairn glasses (Woodhead and Devey, 1993),
430 are among the lowest reported (Fig. 7): Cl/K₂O ratios are less than 0.05 in our São Miguel
431 inclusions, similar to values of pristine melt reported for the Austral Islands (Lassiter et al.
432 2002), and thus lower than the suggested ‘cut-off’ value of 0.05 for MORB (Michael and
433 Cornell, 1998; Shimizu et al., 2016). Above this value, melts are argued to have experienced
434 assimilation of seawater-derived materials, such as altered oceanic crust. Thus, we suggest
435 that there is no detectable assimilated Cl in the melt inclusions, and the Cl and K₂O
436 compositions represent those of the primitive melts.

437 Overall, Cl and F exhibit concentrations comparable to volatile element-rich inclusions from
438 Pico island. A subset of the São Miguel inclusions (excluding degassed samples) have
439 Cl/K₂O ratios in the range of Pico melt inclusions (Fig. 6). Furthermore, F/Nd values of Pico
440 melt inclusions are identical to F/Nd of São Miguel melt inclusions, and the relative trace
441 element abundances of melt inclusions from São Miguel and Pico also similar. Based on
442 these similarities, the mantle beneath São Miguel is inferred to be as volatile-rich as that
443 beneath Pico, and we propose that the volatile-rich mantle source of the Azores hotspot
444 (found under the MAR and Pico island) extends westward beneath São Miguel (e.g. Asimow
445 et al., 2004; Métrich et al., 2014).

446 5.2.3. Sulfur, iron and Pb isotope variations

447 The S concentrations of São Miguel melt inclusions correlate positively with FeO
448 (correlation coefficient =0.72; Fig. 8). Such a correlation is often interpreted as resulting from
449 sulfide saturation in the magma because S solubility increases with increasing FeO content

450 (e.g. Li and Naldrett, 1993; O'Neill and Mavrogenes, 2002). Several models are available for
451 investigation of S saturation in São Miguel melt inclusions. Sulfide saturation in magmas can
452 be determined with models parameterized for P, T, composition, and $f(\text{O}_2)$ (Wallace and
453 Carmichael, 1992; more recent models, however, do not employ oxygen fugacity; Liu et al.,
454 2007; Li and Ripley, 2009), as well as H_2O content (Fortin et al., 2015). Here, we use the
455 model of Fortin et al. (2015) to determine sulfur concentration at sulfide saturation (SCSS)
456 corresponding to the melt inclusions ($T=1200^\circ\text{C}$, and P calculated by MagmaSat with
457 $f(\text{O}_2)=\text{QFM}+1$); note that for samples with no H_2O measurements, we assumed $\text{H}_2\text{O}=1552$
458 ppm, the maximum measured H_2O content in our São Miguel melt inclusions. The S
459 saturation conditions are represented (Fig. 9) by an uncertainty band delimited by dotted lines,
460 which represents a variation of $\pm 50\%$ around an ideal value, where the ideal value refers to
461 the thermodynamic equilibrium value (see Fig. 6b of Fortin et al., 2015, in which $\pm 50\%$ was
462 assessed by the relative difference between modelled S and measured S concentrations for
463 natural samples with less than 2000 ppm S). Model results indicate that only two melt
464 inclusions plot outside of the sulfide saturation band (ACO95-62i, its replicate measurement,
465 and 2000-9-4). All other melt inclusions analysed follow a linear-trend parallel to the 1:1 line
466 (Fig. 9). If the H_2O concentration (1552 ppm) is increased to 2 wt% (maximum H_2O
467 concentration in Pico melt inclusions; Métrich et al., 2014), the modelled S concentrations of
468 São Miguel melt inclusions increase by 20% but remain within the S saturation uncertainty
469 band. If temperature is decreased to 1150°C , the SCSS decreases by 13% and the São Miguel
470 melt inclusions plot closer to the 1:1 line. Pressure is not a sensitive parameter in this model.
471 Based on these calculations, sulfur concentrations in the majority of São Miguel melt
472 inclusions are at sulfide saturation. The two sulfide-undersaturated melt inclusions have
473 lower S concentrations ($<400\text{ppm}$). Therefore, the sulfur content of these S-undersaturated
474 samples is likely controlled by degassing (i.e. sulfate formation), and not by sulfide
475 saturation. The following discussion excludes these two S-undersaturated melt inclusions.
476 The correlation between S concentrations and Pb isotopic compositions in the melt inclusions
477 is enigmatic (Fig. 8). Here, the correlation implies a relationship between two geochemical
478 processes: sulfide saturation (dissolution/precipitation) and the mixing of at least two distinct
479 Pb-isotopic components. Because precipitation of sulfide within melt inclusions cannot
480 account for this correlation, the isotopically distinct magma compositions must have been
481 present prior to melt inclusion entrapment. Accounting for these conditions, we propose a
482 scenario where sulfide blebs with unradiogenic Pb-isotopic compositions (high $^{207}\text{Pb}/^{206}\text{Pb}$)

483 dissolve to various extents into São Miguel melts before the melts are trapped in olivines.
484 Two critical assumptions are required for this model, which are the presence of (1) a sulfide-
485 undersaturated magma, and (2) Pb-rich sulfides with high $^{207}\text{Pb}/^{206}\text{Pb}$. The first assumption is
486 valid since the solubility of S increases with decreasing pressure (e.g. Fortin et al., 2015); the
487 S content of magma formed in the mantle will most likely be undersaturated at shallower
488 depth (for example in a magma chamber). For our second hypothesis, the existence of a high
489 $^{207}\text{Pb}/^{206}\text{Pb}$ signature in sulfide is not an exotic idea (e.g. Warren and Shirey, 2012) and high
490 values for Pb partition coefficients between sulfide and melt (e.g. Kiseeva and Wood, 2013;
491 Patten et al., 2013; Hart and Gaetani, 2016) now suggest some sulfides can have high Pb
492 concentrations. If such a S-undersaturated melt can interact with sulfides present in a
493 lithology predating the sulfide-undersaturated magma (for example sulfides in the wall of the
494 magma chamber, genetically unrelated to the S-undersaturated magma), each with distinct Pb
495 isotope compositions, a mixing model can quantitatively test the amount of sulfide dissolved
496 into the magma. This sulfide dissolution process can generate variability in Pb
497 concentrations, S concentrations, and Pb isotopic ratios. A similar idea of oceanic crust (or
498 oceanic lithosphere)-sulfide dissolution/destabilisation has recently been proposed to explain
499 the disequilibrium of Pb isotopes between Fe oxides and their host rocks in Reunion Island
500 (Vlastélic et al., 2016). We apply a binary mixing model between a sulfide melt and a basaltic
501 magma. The sulfide endmember composition is chosen as FeS (36 wt. % S). The basaltic
502 magma composition has a concentration of 500 ppm S (corresponding to the minimum S
503 measured in São Miguel melt inclusions, excluding the degassed melt inclusion). The lead
504 isotope end members are $^{207}\text{Pb}/^{206}\text{Pb} = 0.857$ for sulfides (representing oceanic crust) and
505 $^{207}\text{Pb}/^{206}\text{Pb} = 0.780$ for the basaltic Nordeste component (the lowest $^{207}\text{Pb}/^{206}\text{Pb}$ value a melt
506 inclusion can reach; Table 1). Model results show the observed Pb-isotope and S
507 concentration variations in São Miguel melt inclusions are explained by less than 0.4% of
508 sulfide incorporation (Fig. 8; similar to the sulfide fraction proposed for Réunion island,
509 Vlastélic et al., 2016). The mixing proportion of sulfide is sufficiently low that major and
510 incompatible (and non-chalcophile) trace element compositions remain unchanged and
511 identical to the magma derived from the São Miguel mantle. However, this mixing will
512 change the Pb isotopic composition, S abundance, and the abundances of all chalcophile
513 elements, because Pb is a strongly chalcophile element in magmatic systems (e.g., Hart and
514 Gaetani, 2006; 2016; Kiseeva and Wood, 2015; Wood and Kiseeva, 2015).

515 Lead concentrations of the endmembers are derived as follows. Because Pb concentrations
516 were not measured in this study, we estimated the range of Pb concentrations in the melt
517 inclusions using Ce/Pb of São Miguel lavas (from 21 to 30: Georoc database, filtered for SiO₂
518 between 42 and 53 wt. %). From measured Ce concentrations, Pb concentrations in the melt
519 inclusions are estimated to be between 2 to 6 ppm. A value of 2 ppm Pb is used for the
520 modelled basaltic magma endmember to have a lower estimate of Pb concentration in
521 sulfides. The sulfide endmember must have formed from a cooling magma at the time of
522 oceanic crust formation. Therefore, the concentration of Pb in the sulfide is determined using
523 a Pb partition coefficient ($D_{\text{Pb}}^{\text{sulfide/melt}}$) and a mantle derived basalt with 2 ppm Pb, and it
524 ranges from 60 and 280 ppm Pb using $D_{\text{Pb}}^{\text{sulfide/melt}}$ of 30 and 140, respectively. These
525 partition coefficients are determined by extrapolation of the parameterisation of Hart and
526 Gaetani (2016). For comparison, $D_{\text{Pb}}^{\text{sulfide/melt}}$ values ranging from 45 to 73 were measured
527 between sulfide droplets and coexisting natural MORB glasses (Patten et al., 2013) and the
528 model of Kiseeva and Wood (2013) gives 25 to 98 depending on the measured FeO contents
529 of our melt inclusions. Because $D_{\text{Pb}}^{\text{sulfide/melt}}$ is a function of pressure, where D is higher at
530 low pressure, the oceanic crust sulfide with high Pb concentration is inferred to have formed
531 at low pressure (< 0.5 GPa). It should be noted that low Pb abundances are found in sulfides
532 from abyssal peridotites (average 4 ppm; Warren and Shirey, 2012), where sulfides are
533 thought to form at high pressure (low $D_{\text{Pb}}^{\text{sulfide/melt}}$) before emplacement at the ocean floor.

534 Os is also a chalcophile element (e.g. Brennan, 2008), but Os isotopes show little variation in
535 São Miguel lavas (Widom et al., 1996), perhaps because, unlike Pb, there is little Os isotopic
536 variability between the Azores mantle plume and the dissolving sulfides. Since sulfide does
537 not carry Sr or Nd, the sulfide dissolution model would not generate correlation of Pb
538 isotopes with Sr and Nd isotopes. This sulfide dissolution model for our melt inclusion study
539 could be in contradiction with previous observations of whole rock correlations of Pb-
540 isotopes with Sr and Nd isotopes (e.g. Beier et al., 2007; Elliott et al., 2007). However, it has
541 been suggested that Pb isotopes are de-coupled from Sr and Nd isotopes, which are more
542 silicate-controlled isotopic tracers (e.g. Hart and Gaetani, 2006). Upon close inspection, the
543 model of Beier et al. (2007) requires the presence of mafic material in both Central and
544 Nordeste source mantles. Incorporation of our sulfide dissolution model into the model of
545 Beier et al. (2007) would not cause a contradiction, supposing that the Pb isotopic
546 composition of the Central Group mafic component is abundant in the oceanic crust sulfide.

547 We rule out other mixing hypotheses that could account for the correlation of S
548 concentrations and Pb isotopes. For example, if magma mixing occurs between low FeO
549 (evolved) and high FeO (primitive) magmas with different endmember Pb isotopic
550 compositions, and if the melts were sulfide saturated, a correlation between FeO, S, and Pb
551 isotopic ratios might be expected. However, this mixing scenario should lead to a linear
552 correlation between every chemical component (e.g. major elements), a characteristic not
553 observed in the São Miguel melt inclusion dataset.

554 5.3. F/Nd characteristics of melt inclusions from OIB magmas

555 It has been suggested that F/Nd in melt inclusions and glasses from MORB and OIB is
556 relatively constant (average value of 21 ± 5 from Workman et al., 2006) because there is no
557 significant F/Nd fractionation during crystallization and melting. These two incompatible
558 elements have similar bulk partition coefficients during mantle melting (e.g. Dalou et al.,
559 2011). Hence, F/Nd is a canonical ratio that can be used to trace mantle sources. Specifically,
560 using basalt–bulk peridotite partition coefficients, $D_F/D_{Nd} = 0.056/0.044 = 2.24$ (values from
561 Dalou et al., 2014; and alphaMELTS default routine), the concentration ratio of F/Nd in the
562 melt deviates less than 20% from the source ratio when the degree of partial melting exceeds
563 0.5%. An average of São Miguel melt inclusions gives $F/Nd = 23.1 \pm 3.4$ (1σ) (Figs. 7, 10).
564 The relative constancy of the F/Nd value suggests that there is a single parental magma
565 beneath São Miguel with F/Nd of 23.1 ± 3.4 . As was the case for other trace element ratios,
566 F/Nd does not correlate with Pb isotopic compositions in the São Miguel melt inclusion suite.

567 Pb isotope compositions represent a classical geochemical tracer of mantle sources of hotspot
568 lavas. Mantle endmembers such as HIMU (e.g. Mangaia), EMI (e.g. Pitcairn) and EMII (e.g.
569 Samoa) are considered endmembers based on their extreme isotope compositions among
570 hotspot lavas erupted globally (e.g. Zindler and Hart, 1986; Hofmann, 1997; White, 2015).
571 F/Nd ratios in melt inclusions can potentially characterize the mantle source of melts, similar
572 to Pb isotopic ratios. Therefore, comparing both F/Nd and Pb isotope measurements from
573 different OIBs would illustrate F heterogeneity in the mantle. Fig. 10 shows a broad negative
574 correlation between F/Nd and $^{207}\text{Pb}/^{206}\text{Pb}$ defined by melt inclusions and glasses from OIBs
575 defining mantle endmembers, confirming that F/Nd records mantle heterogeneity (e.g.
576 Lassiter et al. 2002; Koleszar et al., 2009; Rose-Koga et al., 2012; Jackson et al., 2015). For
577 example, oceanic melts with radiogenic Pb-isotopic compositions (high $^{206}\text{Pb}/^{204}\text{Pb}$, or low
578 $^{208}\text{Pb}/^{206}\text{Pb}$ and low $^{207}\text{Pb}/^{206}\text{Pb}$) tend to have elevated F/Nd ratios, and oceanic melts with less

579 radiogenic Pb-isotopic compositions (low $^{206}\text{Pb}/^{204}\text{Pb}$, or high $^{208}\text{Pb}/^{206}\text{Pb}$ and high $^{207}\text{Pb}/^{206}\text{Pb}$)
580 tend to have lower F/Nd ratios. Mangaia melt inclusions, which have the most radiogenic
581 (HIMU) Pb isotopic compositions globally, have relatively high F/Nd, between 20 and 40
582 (Cabral et al., 2014; Fig.7). São Miguel inclusions are consistent with this relationship: the
583 slight HIMU signature of São Miguel melt inclusions is reflected by the relatively high F/Nd
584 (18 to 27). São Miguel melt inclusions have F/Nd overlapping that of Samoa basaltic glasses
585 (representative of EMII, Fig.10), consistent with the influence of an enriched endmember
586 component in the source of São Miguel. EMI has lower F/Nd (between 14 and 20,
587 represented by Pitcairn glasses; Fig. 8) that is similar to MORB.

588 The origin of the global relationship between F/Nd and Pb-isotopic compositions may relate
589 to both (i) the recycled protoliths (oceanic crust, sediments, etc.) that are subducted and
590 mixed into the mantle sources of different hotspots and (ii) the recycling efficiency of F.
591 While F and Cl likely have elevated concentrations in a subducting slab (e.g. Straub and
592 Layne, 2003; Debret et al., 2013), both are likely lost from the slab during dehydration or
593 melting at subduction zones (Kendrick et al., 2011, 2012 for Cl; Kendrick et al., 2014 for F).
594 If ancient subducted oceanic crust is responsible for the generation of radiogenic Pb isotopic
595 reservoirs (e.g. HIMU) in the mantle (e.g. Hofmann and White, 1982; Hauri and Hart, 1993;
596 Hanyu et al., 2011), then the elevated F/Nd in oceanic lavas with a radiogenic signature
597 suggests that F is retained (with respect to Nd) in the slab during subduction. In contrast,
598 oceanic lavas sampling the EMI and EMII reservoirs tend to have lower F/Nd, which
599 suggests that the protoliths (pelagic sediments, terrigenous sediments, lower continental crust,
600 etc.) were more efficiently stripped of their complement of F than the HIMU domain. The
601 process that leads to different degrees of F retention relative to Nd during subduction is not
602 well known, but must relate to variable F loss from the subducting slab, possibly as a
603 function of different temperatures and bulk lithologies (sediments versus oceanic crust, etc.;
604 see Van den Bleeken and Koga, 2015). Upon dehydration, the hydroxyl site in silicate
605 minerals – which has a strong affinity for F (e.g., Smith et al., 1981; Wu and Koga, 2013) –
606 provides an ideal mineralogical site to promote recycling of F. Thus, following prograde
607 metamorphism, residual subducted mafic slab mineralogies with amphibole, mica, and/or
608 apatite would be conducive to efficient transport of F into the deeper mantle with the
609 downgoing slab. However, partial melting of the subducting slab sediments would promote
610 efficient transport of F (along with Nd) to the mantle wedge, depleting the slab of its
611 complement of F (e.g. Rose-Koga et al., 2014). Indeed, thermal models suggest the top

612 portion of the slab to be the hottest, and sediments have a lower solidus temperature than
613 oceanic crust (e.g. Peacock, 1990; Van Keken et al., 2002). This model may help explain why
614 enriched mantle reservoirs that host recycled sediments will be depleted in F (lower F/Nd),
615 while HIMU mantle reservoirs hosting recycling oceanic crust will be less depleted in F
616 (higher F/Nd).

617

618 **6. Conclusions**

619 São Miguel olivine-hosted melt inclusions suggest a single initial lithology beneath
620 the island based on three lines of evidence. (1) The major element compositions of the
621 inclusions cluster towards the low SiO₂ range of the entire São Miguel whole rock trend. (2)
622 Trace element patterns are tightly clustered and parallel. However, despite this uniform trace
623 element composition, variations in Pb isotopic compositions are interpreted following the
624 scenario for the whole rock, as mixing between a non-radiogenic component, “the Central
625 Group Component”, and a radiogenic component called “the Nordeste Component”. (3)
626 Based on undegassed F and Cl, the source beneath São Miguel is volatile-rich, therefore the
627 “wet” source beneath Pico island (Métrich et al., 2014) extends eastward under São Miguel.

628 The Pb-isotopic compositions of the melt inclusions correlate positively with S
629 concentrations. This is tentatively interpreted as being due to small sulfide blebs (isotopically
630 distinct with respect to Pb) located in the oceanic crust of the Central Group component that
631 are dissolved by a S-undersaturated Nordeste component magma. This process does not
632 significantly affect the major and trace element contents of the melt inclusions, but drastically
633 modifies the Pb isotope compositions and S concentrations.

634 Refining the volatile element chemical characteristics of the melt inclusions, we
635 defined characteristic Cl/K₂O=0.035±0.011 and F/Nd=23.1±3.4 for the parental magma of
636 São Miguel island.

637 Comparing melt inclusions from OIBs representing mantle endmembers, we show a
638 global negative correlation between F/Nd and Pb isotope composition of melt inclusions. São
639 Miguel melt inclusions have intermediate F/Nd, between the lower F/Nd of Pitcairn melt
640 inclusions (representing EMI, between 14 to 20) and the higher F/Nd of Mangaia melt
641 inclusions (representing HIMU, between 20 and 41).

642

643 Acknowledgements: ER-K thanks JL Devidal for his precious guidance and discussions
644 during the electron probe analysis. Many thanks go to ER & FR having often kept
645 “distractions” away during the writing of this manuscript. Thank you to R. Dennen for

646 English editing (RD Editing Services). ER-K acknowledges financial support from the CNRS
647 (Institut National des Sciences de l'Univers). This research was financed by the French
648 Government Laboratory of Excellence initiative n°ANR-10-LABX-0006, the Région
649 Auvergne and the European Regional Development Fund. MGJ acknowledges NSF grant
650 EAR-1347377. This is Laboratory of Excellence ClerVolc contribution number XXX. The
651 NordSIMS facility is financed and operated under a joint Nordic contract; this is NordSIMS
652 contribution no. XXX.

653

654 References

- 655 Abdel-Monem, A. A., L. A. Fernandez and G. M. Boone, 1975, "K-Ar ages from the eastern
656 Azores group (Santa Maria, São Miguel and the Formigas Islands)." *Lithos*, 8, 247-254.
- 657 Agranier, A., Blichert-Toft, J., Graham, D., Debaille, V., Schiano, P., and Albarede, F., 2005,
658 The spectra of isotopic heterogeneities along the mid-Atlantic Ridge: *Earth and Planetary
659 Science Letters*, 238, 96–109, doi: doi:10.1016/j.epsl.2005.07.011.
- 660 Asimow, P.D., Dixon, J.E., and Langmuir, C.H., 2004, A hydrous melting and fractionation
661 model for mid-ocean ridge basalts: Application to the Mid-Atlantic Ridge near the Azores,
662 *Geochemistry Geophysics Geosystems*, 5, doi: 10.1029/2003GC000568.
- 663 Beier, C., Haase, K.M., and Hansteen, T.H., 2006, Magma Evolution of the Sete Cidades
664 Volcano, São Miguel, Azores: 47, 1375–1411.
- 665 Beier, C., Stracke, A., and Haase, K., 2007, The peculiar geochemical signatures of São
666 Miguel (Azores) lavas: Metasomatised or recycled mantle sources?: *Earth and Planetary
667 Science Letters*, 259, 186–199.
- 668 Beier, C., Haase, K., and Turner, S., 2012, Conditions of melting beneath the Azores: *Lithos*,
669 144-145, 1–11.
- 670 Bourdon, B., Turner, S.P., and Ribe, N.M., 2005, Partial melting and upwelling rates beneath
671 the Azores from a U-series isotope perspective, *Earth and Planetary Science Letters*, 239, 42–
672 56.
- 673 Brenan, J.M., 2008, Re–Os fractionation by sulfide melt–silicate melt partitioning: A new
674 spin: *Chemical Geology*, 248, 140–165.
- 675 Bucholz, C.E., Gaetani, G.A., and Behn, M.D., 2013, Post-entrapment modification of
676 volatiles and oxygen fugacity in olivine-hosted melt inclusions: *Earth and Planetary Science
677 Letters*, 374, 145–155.
- 678 Cabral, R.A., Jackson, M.G., Koga, K.T., Rose-Koga, E.F., Hauri, E.H., Whitehouse, M.J.,
679 Price, A.A., Day, J.M.D., Shimizu, N., and Kelley, K.A., 2014, Volatile cycling of H₂O, CO
680 2, F, and Cl in the HIMU mantle: A new window provided by melt inclusions from oceanic
681 hot spot lavas at Mangaia, Cook Islands: *Geochemistry Geophysics Geosystems*, 15, 4445–
682 4467, doi: 10.1002/2014GC005473.
- 683 Chen, Y., Provost, A., Schiano, P., and Cluzel, N., 2011, The rate of water loss from olivine-
684 hosted melt inclusions: *Contributions to Mineralogy and Petrology*, 162, 625–636, doi:
685 10.1007/s00410-011-0616-5.
- 686 Dalou, C., Koga, K.T., Shimizu, N., Boulon, J., and Devidal, J.-L., 2011, Experimental

687 determination of F and Cl partitioning between lherzolite and basaltic melt: Contributions to
688 Mineralogy and Petrology, 163, 591–609, doi: 10.1007/s00410-011-0688-2.

689 Danyushevsky, L., Della-Pasqua, F., and Sokolov, S., 2000, Re-equilibration of melt
690 inclusions trapped by magnesian olivine phenocrysts from subduction-related magmas:
691 petrological implications: Contributions to Mineralogy and Petrology, 138, 68–83.

692 Danyushevsky, L.V., McNeill, A.W., and Sobolev, A.V., 2002, Experimental and
693 petrological studies of melt inclusions in phenocrysts from mantle-derived magmas: an
694 overview of techniques, advantages and complications, Chemical Geology, 183, 5-24.

695 Davies, G.R., Cliff, R.A., Norry, M.J., and Gerlach, D.C., 1989, A combined chemical and
696 Pb-Sr-Nd isotope study of the Azores and Cape Verde hot-spots: the geodynamic
697 implications: Geological Society, London, Special Publications, 42, 231–255, doi:
698 10.1144/GSL.SP.1989.042.01.15.

699 Debret, B., Koga, K.T., Nicollet, C., Andreani, M., and Schwartz, S. (2013) F, Cl and S input
700 via serpentinite in subduction zones: implications for the nature of the fluid released at depth:
701 Terra Nova, p. n/a–n/a, doi: 10.1111/ter.12074.

702 Dixon, J.E., Clague, D.A. and Stolper, E.M. (1991) Degassing History of Water, Sulfur, and
703 Carbon in Submarine Lavas from Kilauea Volcano, Hawaii (1991), The Journal of Geology,
704 99, 371-394

705 Dixon, J.E., and Stolper, E.M., 1995, An experimental study of water and carbon dioxide
706 solubilities in mid-ocean ridge basaltic liquids. Part II: applications to degassing: Journal of
707 Petrology, 36, 1633–1646.

708 Elliott, T., Blichert-Toft, J., Heumann, A., Koetsier, G., and Forjaz, V., 2007, The origin of
709 enriched mantle beneath São Miguel, Azores: Geochimica et Cosmochimica Acta, 71, 219–
710 240, doi: 10.1016/j.gca.2006.07.043.

711 Fortin, M.-A., Riddle, J., Desjardins-Langlais, Y., and Baker, D.R., 2015, The effect of water
712 on the sulfur concentration at sulfide saturation (SCSS) in natural melts, Geochimica et
713 Cosmochimica Acta, 160, 100–116, doi: 10.1016/j.gca.2015.03.022.

714 French, S.W., and Romanowicz, B., 2015, Broad plumes rooted at the base of the Earth's
715 mantle beneath major hotspots: Nature, 525, 95–99, doi: doi:10.1038/nature14876.

716 Gaetani, G.A., and Watson, E.B., 2000, Open system behavior of olivine-hosted melt
717 inclusions: Earth and Planetary Science Letters, 183, 27–41.

718 Gaetani, G.A., O'Leary, J.A., Shimizu, N., Bucholz, C.E., and Newville, M., 2012, Rapid
719 reequilibration of H₂O and oxygen fugacity in olivine-hosted melt inclusions: Geology, v.
720 40, no. 10, p. 915–918, doi: 10.1130/G32992.1.

721 Gaetani, G.A., O'Leary, J.A., Koga, K.T., Hauri, E.H., Rose-Koga, E.F., and Monteleone,
722 B.D., 2014, Hydration of mantle olivine under variable water and oxygen fugacity
723 conditions: Contributions to Mineralogy and Petrology, 167, 965–14, doi: 10.1007/s00410-
724 014-0965-y.

725 Gale A., C. A. Dalton, C. H. Langmuir, Y. Su, and J.-G. Schilling (2013), The mean
726 composition of ocean ridge basalts, Geochem. Geophys. Geosyst., 14, 489–518,
727 doi:10.1029/2012GC004334.

728

729 Gao, S., Liu, X., Yuan, H., Hattendorf, B., Günther, D., Chen, L., and Hu, S., 2007,
730 Determination of Forty Two Major and Trace Elements in USGS and NIST SRM Glasses by
731 Laser Ablation-Inductively Coupled Plasma-Mass Spectrometry: Geostandards and
732 Geoanalytical Research, 26, 181–196, doi: 10.1111/j.1751-908X.2002.tb00886.x.

733 Ghiorso, M.S., 2015, MagmatSat app. Available through apple store.

734 Hauri, E. & Hart, S. R., 1993, Re-Os isotope systematics of HIMU and EMII oceanic island
735 basalts from the south Pacific Ocean. *Earth Planetary Science Letters* 114, 353–371.

736 Hanyu, T., Tatsumi, Y., and Kimura, J.-I., 2011, Constraints on the origin of the HIMU
737 reservoir from He–Ne–Ar isotope systematics: *Earth and Planetary Science Letters*, v. 307,
738 no. 3-4, p. 377–386, doi: 10.1016/j.epsl.2011.05.012.

739 Hart, S.R., and Gaetani, G.A., 2006, Mantle Pb paradoxes: the sulfide solution: *Contributions*
740 *to Mineralogy and Petrology*, 152, 295–308, doi: 10.1007/s00410-006-0108-1.

741 Hart, S.R., and Gaetani, G.A., 2016, Experimental determination of Pb partitioning between
742 sulfide melt and basalt melt as a function of P, T and X: *Geochimica et Cosmochimica Acta*,
743 doi: 10.1016/j.gca.2016.01.030.

744 Hawkesworth, C.J., Norry, M.J., Roddick, J.C., and Vollmer, R., 1979, 143Nd/144Nd and
745 87Sr/86Sr ratios from the Azores and their significance in LIL-element enriched mantle:
746 *Nature*, 280, 28–31, doi: 10.1038/280028a0.

747 Helo, C., Longpré, M.-A., Shimizu, N., Clague, D.A., and Stix, J., 2011, Explosive eruptions
748 at mid-ocean ridges driven by CO₂-rich magmas: *Nature Geoscience*, 4, 260–263, doi:
749 10.1038/ngeo1104.

750 Hofmann, A.W., 1997, Mantle geochemistry: the message from oceanic volcanism: *Nature*, v.
751 385, no. 6613, p. 219–229.

752 Jackson M.G., Koga K.T., Price A., Konter J.G., Koppers A.A.P., Finlayson V.A., Konrad K.,
753 Hauri E.H., Kylander-Clark A., Kelley K.A., Kendrick M.A., 2015, Deeply-dredged
754 Submarine HIMU Glasses from the Tuvalu Islands, Polynesia: Implications for Volatile
755 Budgets of Recycled Oceanic Crust, Paper #2015GC005966R, in press *Geochemistry*
756 *Geophysics Geosystems*.

757 Jochum, K.P., Stoll, B., Herwig, K., Willbold, M., Hofmann, A.W., Amini, M., Aarburg, S.,
758 Abouchami, W., Hellebrand, E., Mocek, B., Raczek, I., Stracke, A., Alard, O., Bouman, C.,
759 et al., 2006, MPI-DING reference glasses for in situ microanalysis: New reference values for
760 element concentrations and isotope ratios: *Geochemistry Geophysics Geosystems*, 7, doi:
761 10.1029/2005GC001060.

762 Johnson, C. L., J. R. Wijbrans, C. G. Constable, J. Gee, H. Staudigel, L. Tauxe, V.-H. Forjaz
763 and M. Salgueiro, 1998, "40Ar/39Ar ages and paleomagnetism of Sao Miguel lavas, Azores."
764 *Earth and Planetary Science Letters* 160: 637-649.

765 Kelley, K.A., Kingsley, R., and Schilling, J.-G., 2013, Composition of plume-influenced
766 mid-ocean ridge lavas and glasses from the Mid-Atlantic Ridge, East Pacific Rise, Galápagos
767 Spreading Center, and Gulf of Aden: *Geochemistry Geophysics Geosystems*, 14, 223–242,
768 doi: 10.1002/ggge.20049.

769 Kendrick, M.A. Scambelluri, M., Honda, M., and Phillips, D., 2011, High abundances of
770 noble gas and chlorine delivered to the mantle by serpentinite subduction : *Nature*
771 *Geoscience* : Nature Publishing Group: *Nature Geoscience*, v. 4, p. 807–812, doi:
772 10.1038/NGEO1270.

- 773 Kendrick, M.A., Woodhead, J.D., and Kamenetsky, V.S., 2012, Tracking halogens through
774 the subduction cycle: *Geology*, v. 40, no. 12, p. 1075–1078, doi: 10.1130/G33265.1.
- 775 Kendrick, M.A., Jackson, M.G., Kent, A.J.R., Hauri, E.H., Wallace, P.J., and Woodhead, J.,
776 2014, Contrasting behaviours of CO₂, S, H₂O and halogens (F, Cl, Br, and I) in enriched-
777 mantle melts from Pitcairn and Society seamounts: *Chemical Geology*, 370, 69–81, doi:
778 10.1016/j.chemgeo.2014.01.019.
- 779 Kiseeva, E.S., and Wood, B.J., 2015, The effects of composition and temperature on
780 chalcophile and lithophile element partitioning into magmatic sulphides: *Earth and Planetary
781 Science Letters*.
- 782 Koleszar, A.M., Saal, A.E., Hauri, E.H., Nagle, A.N., Liang, Y., and Kurz, M.D., 2009, The
783 volatile contents of the Galapagos plume; evidence for H₂O and F open system behavior in
784 melt inclusions: *Earth and Planetary Science Letters*, 287, 442–452, doi:
785 10.1016/j.epsl.2009.08.029.
- 786 Kurz M.D., 1993, Mantle heterogeneity beneath ocean islands: some inferences from :
787 isotopes. *Philos. Trans. R. Soc. London* 342, 91-103.
- 788 Lassiter, J., Hauri, E.H., Nikogosian, I., and Barszczus, H., 2002, Chlorine–potassium
789 variations in melt inclusions from Raivavae and Rapa, Austral Islands: constraints on
790 chlorine recycling in the mantle and evidence for brine-induced melting of oceanic crust:
791 *Earth and Planetary Science Letters*, 202, 525–540.
- 792 Le Bas, M.J.L., Lemaitre, R.W.L., Streckeisen, A., Zanettin, B., and Rocks, 1986, A
793 Chemical Classification of Volcanic Rocks Based on the Total Alkali-Silica Diagram,
794 *Journal of Petrology*, 27, 745–750.
- 795 Le Voyer, M., Rose-Koga, E.F., Laubier, M., and Schiano, P., 2008, Petrogenesis of arc lavas
796 from the Rucu Pichincha and Pan de Azucar volcanoes (Ecuadorian arc): Major, trace
797 element, and boron isotope evidences from olivine-hosted melt inclusions: *Geochemistry
798 Geophysics Geosystems*, 9, doi: 10.1029/2008GC002173.
- 799 Le Voyer, M., Rose-Koga, E.F., Shimizu, N., Grove, T.L., and Schiano, P., 2010, Two
800 Contrasting H₂O-rich Components in Primary Melt Inclusions from Mount Shasta: *Journal of
801 Petrology*, 51, 1571–1595, doi: 10.1093/petrology/egq030.
- 802 Le Voyer, M., E. Cottrell, K. A. Kelley, M. Brounce, and E. H. Hauri, 2015, The effect of
803 primary versus secondary processes on the volatile content of MORB glasses: An example
804 from the equatorial Mid-Atlantic Ridge (5°N–3°S), *J. Geophys. Res. Solid Earth*, 120, 125–
805 144, doi:10.1002/2014JB011160.
- 806 Li and Naldrett, 1993 Sulfide capacity of magma; a quantitative model and its application to
807 the formation of sulfide ores at Sudbury, Ontario, *Economic Geology*, 88, 1253-1260
- 808 Li and Ripley, 2009, Sulfur Contents at Sulfide-Liquid or Anhydrite Saturation in Silicate
809 Melts: Empirical Equations and Example Applications, *Economic Geology*, 104, 405-412
- 810 Liu, Y., Samaha, N.-T., and Baker, D.R., 2007, Sulfur concentration at sulfide saturation
811 (SCSS) in magmatic silicate melts, *Geochimica et Cosmochimica Acta*, 71, 1783–1799, doi:
812 10.1016/j.gca.2007.01.004.
- 813 Madureira, P., Moreira, M., Mata, J., and Nunes, J.C., 2014, Helium isotope systematics in
814 the vicinity of the Azores triple junction: Constraints on the Azores geodynamics, *Chemical
815 Geology*, 372, 62–71.
- 816 Métrich, N., Zanon, V., Créon, L., Hildenbrand, A., Moreira, M., and Marques, F.O., 2014, Is

- 817 the “Azores Hotspot” a Wetspot? Insights from the Geochemistry of Fluid and Melt
818 Inclusions in Olivine of Pico Basalts, *Journal of Petrology*, 55, 377–393.
- 819 Michael, P.J., 1988, The concentration, behavior and storage of H₂O in the suboceanic upper
820 mantle, Implications for mantle metasomatism, *Geochimica et Cosmochimica Acta*, 52, 555-
821 566.
- 822 Michael, P.J., and Cornell, W.C., 1998, Influence of spreading rate and magma supply on
823 crystallization and assimilation beneath mid-ocean ridges: Evidence from chlorine and major
824 element chemistry of mid-ocean ridge basalts, *Journal of Geophysical Research*, 103, 18325–
825 18–356.
- 826 Millet, M.-A., R. Doucelance, J. A. Baker and P. Schiano (2009). "Reconsidering the origins
827 of isotopic variations in Ocean Island Basalts: Insights from fine-scale study of São Jorge
828 Island, Azores archipelago." *Chemical Geology* 265: 289-302.
- 829 Moore, R.B., 1990, Volcanic geology and eruption frequency, São Miguel, Azores, *Bulletin*
830 *of Volcanology*, 52, 602–614.
- 831 Moreira, M., Doucelance, R., Kurz, M., and Dupre, B., 1999, Helium and lead isotope
832 geochemistry of the Azores Archipelago: *Earth and Planetary Science Letters*, 169, 189–205.
- 833 Moreira, M., Kanzari, A. and Madureira, P., 2012, Helium and neon isotopes in São Miguel
834 island basalts, Azores Archipelago: New constraints on the “low ³He” hotspot origin,
835 *Chemical Geology*, 322-323, 91–98.
- 836 O’Neill HS, Mavrogenes JA (2002) The sulfide capacity and the sulfur content at sulfide
837 saturation of silicate melts at 1400 °C and 1 bar, *Journal of Petrology* 43:1049-1087
- 838 Patten, C., Barnes, S.J., Mathez, E.A., and Jenner, F.E., 2013, Partition coefficients of
839 chalcophile elements between sulfide and silicate melts and the early crystallization history
840 of sulfide liquid: LA-ICP-MS analysis of MORB sulfide droplets, *Chemical Geology*, 358,
841 170–188.
- 842 Peacock, S.A., 1990, Fluid processes in subduction zones: *Science*, 248, 329–337.
- 843 Rose-Koga E.F., Shimizu N., Devidal J-L, Koga K.T., Le Voyer M., 2008, Investigation of F,
844 S, and Cl Standards by ion Probe and Electron Microprobe, *Eos Trans. AGU*, 89(53), Fall
845 Meet. Suppl., Abstract V31B-2145.
- 846 Rose-Koga, E.F., Koga, K., Schiano, P., and Le Voyer, M., 2012, Mantle source
847 heterogeneity for South Tyrrhenian magmas revealed by Pb isotopes and halogen contents of
848 olivine-hosted melt inclusions, *Chemical Geology*, 334, 266–279.
- 849 Rose-Koga, E.F., Koga, K.T., Hamada, M., HéLouis, T., Whitehouse, M.J., and Shimizu, N.,
850 2014, Volatile (F and Cl) concentrations in Iwate olivine-hosted melt inclusions indicating
851 low-temperature subduction, *Earth, Planets and Space*, 66, 81, doi: 10.1029/2000GL012558.
- 852 Saal, A.E., Hart, S.R., Shimizu, N., Hauri, E.H., Layne, G., and Eiler, J., 2005, Pb isotopic
853 variability in melt inclusions from the EMI–EMII–HIMU mantle end-members and the role
854 of the oceanic lithosphere, *Earth and Planetary Science Letters*, 240, 605–620, doi:
855 10.1016/j.epsl.2005.10.002.
- 856 Salters, V.J.M., and Stracke, A., 2004, Composition of the depleted mantle, *Geochemistry*
857 *Geophysics Geosystems*, 5, doi: 10.1029/2003GC000597.
- 858 Schilling, J.-G., Bergeron, M.B., Evans, R., 1980. Halogens in the mantle beneath the North
859 Atlantic. *Philos. Trans. R. Soc. London* 297, 147-178.

- 860 Seyfried, W.E., Jr, and Ding, K., 1995, The hydrothermal chemistry of fluoride in seawater:
861 *Geochimica et Cosmochimica Acta*, 59, 1063–1071, doi: 10.1016/0016-7037(95)00023-S.
- 862 Shaw, A.M., Hauri, E.H., Fischer, T.P., Hilton, D.R., and Kelley, K.A., 2008, Hydrogen
863 isotopes in Mariana arc melt inclusions: Implications for subduction dehydration and the
864 deep-Earth water cycle: *Earth and Planetary Science Letters*, 275, 138–145, doi:
865 10.1016/j.epsl.2008.08.015.
- 866 Shaw, A.M., Behn, M.D., Humphris, S.E., Sohn, R.A., and Gregg, P.M., 2010, Deep pooling
867 of low degree melts and volatile fluxes at the 85°E segment of the Gakkel Ridge: Evidence
868 from olivine-hosted melt inclusions and glasses, *Earth and Planetary Science Letters*, 289,
869 311–322, doi: 10.1016/j.epsl.2009.11.018.
- 870 Shimizu, K., Saal, A.E., Myers, C.E., Nagle, A.N., Hauri, E.H., Forsyth, D.W., Kamenetsky,
871 V.S., and Niu, Y., 2016, Two-component mantle melting-mixing model for the generation of
872 mid-ocean ridge basalts: Implications for the volatile content of the Pacific upper mantle,
873 *Geochimica et Cosmochimica Acta*, 176, 44–80, doi: 10.1016/j.gca.2015.10.033.
- 874 Smith, J.V., 1981, Halogen and phosphorus storage in the Earth, *Nature*, 289, 762–765, doi:
875 10.1038/289762a0.
- 876 Sobolev, A.V., and Chaussidon, M., 1996, H₂O concentrations in primary melts from supra-
877 subduction zones and mid-ocean ridges: Implications for H₂O storage and recycling in the
878 mantle, *Earth and Planetary Science Letters*, 137, 45–55.
- 879 Spilliaert, N., Métrich, N., and Allard, P., 2006, S–Cl–F degassing pattern of water-rich alkali
880 basalt: Modelling and relationship with eruption styles on Mount Etna volcano, *Earth and*
881 *Planetary Science Letters*, 248, 772–786, doi: 10.1016/j.epsl.2006.06.031.
- 882 Stefano, C.J., Mukasa, S.B., Andronikov, A., and Leeman, W.P., 2011, Water and other
883 volatile systematics of olivine-hosted melt inclusions from the Yellowstone hotspot track,
884 *Contributions to Mineralogy and Petrology*, 161, 615–633, doi: 10.1007/s00410-010-0553-
885 8.Sobolev and Chaussidon, 1996
- 886 Straub, S.M., and Layne, G.D. (2003) The systematics of chlorine, fluorine, and water in Izu
887 arc front volcanic rocks: Implications for volatile recycling in subduction zones: *Geochimica*
888 *et Cosmochimica Acta*, 67, 4179–4203, doi: 10.1016/S0016-7037(03)00307-7.
- 889 Sun, S.S., and McDonough, W.F., 1989, Chemical and isotopic systematics of oceanic
890 basalts: implications for mantle composition and processes: Geological Society, London,
891 *Special Publications*, 42, 313–345, doi: 10.1144/GSL.SP.1989.042.01.19.
- 892 Thordarson, T., Self, S., Oskarsson, N., and Hulsebosch, T., 1996, Sulfur, chlorine, and
893 fluorine degassing and atmospheric loading by the 1783-1784 AD Laki (Skaftar Fires)
894 eruption in Iceland: *Bulletin of Volcanology*, 58, 205–225, doi: 10.1007/s004450050136.
- 895 Toplis, M.J., 2005, The thermodynamics of iron and magnesium partitioning between olivine
896 and liquid: criteria for assessing and predicting equilibrium in natural and experimental
897 systems, *Contributions to Mineralogy and Petrology*, 149, 22–39, doi: 10.1007/s00410-004-
898 0629-4.
- 899 Turner, S., Hawkesworth, C., Rogers, N., and King, P., 1997, U–Th isotope disequilibria and
900 ocean island basalt generation in the Azores: *Chemical Geology*, 139, 145–164.
- 901 Van den Bleeken, G., and Koga, K.T. (2015) Experimentally determined distribution of
902 fluorine and chlorine upon hydrous slab melting, and implications for F–Cl cycling through
903 subduction zones: *Geochimica et Cosmochimica Acta*, 171, 353–373.

904 Van Keken, P.E., 2002, High-resolution models of subduction zones: Implications for
905 mineral dehydration reactions and the transport of water into the deep mantle: *Geochemistry*
906 *Geophysics Geosystems*, 3, doi: 10.1029/2001GC000256.

907 Vlastélic, I., Gannoun, A., Di Muro, A., and Gurioli, L., 2016, Origin and fate of sulfide
908 liquids in hotspot volcanism (La Réunion): Pb isotope constraints from residual Fe-Cu oxides,
909 *Geochimica et Cosmochimica Acta*, doi: <http://dx.doi.org/10.1016/j.gca.2016.08.036>.

910 Vogt, P.R., and Jung, W.Y., 2004, The Terceira Rift as hyper-slow, hotspot-dominated
911 oblique spreading axis: A comparison with other slow-spreading plate boundaries: *Earth and*
912 *Planetary Science Letters*, 218, 77–90.

913 Wallace, P., and Carmichael, I.S.E., 1992, Sulfur in basaltic magmas: *Geochimica et*
914 *Cosmochimica Acta*, 56, 1863–1874, doi: 10.1016/0016-7037(92)90316-B.

915 Wanless, V.D., and Shaw, A.M., 2012, Lower crustal crystallization and melt evolution at
916 mid-ocean ridges: *Nature Geoscience*, 5, 651–655, doi: 10.1038/ngeo1552.

917 Wanless, V.D., Shaw, A.M., Behn, M.D., Soule, S.A., Escartin, J., and Hamelin, C., 2015,
918 Magmatic plumbing at Lucky Strike volcano based on olivine-hosted melt inclusion
919 compositions, *Geochem. Geophys. Geosyst.*, 16, 126–147, doi:10.1002/2014GC005517.

920 Warren, J.M., and Shirey, S.B., 2012, Lead and osmium isotopic constraints on the oceanic
921 mantle from single abyssal peridotite sulfides: *Earth and Planetary Science Letters*, v. 359-
922 360, p. 279–293, doi: 10.1016/j.epsl.2012.09.055.

923 White, W.M., Tapia, M.D.M., and Schilling, J.-G., 1979, The petrology and geochemistry of
924 the Azores Islands: *Contributions to Mineralogy and Petrology*, 69, 201–213, doi:
925 10.1007/BF00372322.

926 White, W.M., 2015, Isotopes, DUPAL, LLSVPs, and Anekantavada: *Chemical Geology*, 419,
927 10–28, doi: 10.1016/j.chemgeo.2015.09.026.

928 Widom, E., and Shirey, S.B., 1996, Os isotope systematics in the Azores: implications for
929 mantle plume sources: *Earth and Planetary Science Letters*, 142, 451–465.

930 Widom, E., Carlson, R., Gill, J., and Schmincke, H.U., 1997, Th-Sr-Nd-Pb isotope and trace
931 element evidence for the origin of the Sao Miguel, Azores, enriched mantle source: *Chemical*
932 *Geology*, 140, 49–68.

933 Widom, E., 2002, Earth science: Ancient mantle in a modern plume: *Nature a-z index*, 420,
934 281–282.

935 Widom, E., and Farquhar, J., 2003, Oxygen isotope signatures in olivines from Sao Miguel
936 (Azores) basalts: implications for crustal and mantle processes: *Chemical Geology*, 193, 237–
937 255.

938 Witham, F., Blundy, J., Kohn, S.C., Lesne, P., Dixon, J., Churakov, S.V., and Botcharnikov,
939 R., 2012, SolEx: A model for mixed COHSCI-volatile solubilities and exsolved gas
940 compositions in basalt, *Computers & Geosciences*, 45, 87–97, doi:
941 10.1016/j.cageo.2011.09.021.

942 Wood, B.J., and Kiseeva, E.S., 2015, Trace element partitioning into sulfide: How lithophile
943 elements become chalcophile and vice versa: *American Mineralogist*, 100, 2371–2379, doi:
944 10.2138/am-2015-5358CCBYNCND.

945 Woodhead, J.D., and Devey, C.W., 1993, Geochemistry of the Pitcairn seamounts, I: source
946 character and temporal trends: *Earth and Planetary Science Letters*, 116, 81–99.

- 947 Workman, R.K., Hauri, E.H., Hart, S.R., Wang, J., and Blusztajn, J., 2006, Volatile and trace
948 elements in basaltic glasses from Samoa: Implications for water distribution in the mantle:
949 Earth and Planetary Science Letters, 241, 932–951, doi: 10.1016/j.epsl.2005.10.028.
- 950 Wu, J., and Koga, K.T., 2013, Fluorine partitioning between hydrous minerals and aqueous
951 fluid at 1GPa and 770–947°C: A new constraint on slab flux: *Geochimica et Cosmochimica*
952 *Acta*, 119, 77–92.
- 953 Zindler, A., Hart, S.R., 1986. Chemical geodynamics. *Annu. Rev. Earth Planet. Sci.*, 14, 493–
954 571, doi:10.1146/annurev.ea.14.050186.002425

955 Figure captions

956 Fig. 1: Simplified map of the Azores archipelago. The names of the islands are abbreviated as
957 follows: Fl stands for Flores, C for Corvo, G for Graciosa, F for Faial, P for Pico, SJ for Sao
958 Jorge, T for Terceira, SMi for Sao Miguel and SMa for Santa Maria. Sample locations are on
959 Sao Miguel Island (37.7667° N, 25.4667° W, the eastern most island of the Azores
960 archipelago). São Miguel is a 50 km long island composed of 5 volcanic complexes: Sete
961 Cidades, Picos, Fogo, Furnas, and Nordeste. Three volcanoes are active (Sete Cidades, Agua
962 de Pau, and Furnas) and the older Nordeste complex is extinct. The six samples we studied
963 came from Picos, Fogo, and Nordeste.

964
965 Fig. 2: Le Bas classification of Azores whole rocks and melt inclusions. Total alkali
966 ($\text{Na}_2\text{O}+\text{K}_2\text{O}$) is plotted as a function of SiO_2 in wt% (Le Bas et al., 1986). Azores whole
967 rocks vary from picrobasalts to trachyte, and the melt inclusions (bigger symbols) represent
968 less evolved magmas, mostly in the fields of basalt and tephrite basanite with some extension
969 towards trachy-basalt to basaltic trachy-andesite.

970
971 Fig. 3: (a) Trace element patterns of São Miguel melt inclusions (thin black lines) of this
972 study, of Pico melt inclusions (thin gray lines), and of an average N-MORB composition
973 (dashed line; normalization to primitive mantle and N-MORB composition are from Sun and
974 McDonough, 1989). Previously reported whole rock data are shown as the shaded area; all
975 whole rock data was filtered for São Miguel basalts ($\text{SiO}_2 < 53$ wt. %; White et al., 1979;
976 Davies et al., 1989; Turner et al., 1997; Beier et al., 2006, 2007; Madureira et al., 2014). The
977 lack of pronounced kinks at Sr and Eu discards notable addition or subtraction of plagioclase.
978 (b) REE patterns of São Miguel melt inclusions (thin solid lines) and whole rocks (shaded
979 area); references are as in (a).

980
981
982 Fig. 4: $^{207}\text{Pb}/^{206}\text{Pb}$ versus $^{208}\text{Pb}/^{206}\text{Pb}$ for São Miguel melt inclusions (ellipse errors represent
983 2σ standard error of the mean) and the corresponding whole rock measured at LMV (larger
984 symbols, errors are largely within the size of the symbols). Pb-isotope compositions of the
985 whole rocks and 19 melt inclusions (not counting duplicates) are represented: samples
986 ACO95-03, ACO95-56, ACO95-62, and ACO95-68 include whole rock measurements and
987 melt inclusions; whole rock Pb isotopes of 2000-4 and 2000-9 were not measured. The 2σ
988 ellipsoid errors for repeat measurements of standard glasses with 19 ppm (GOR132G
989 standard; Jochum et al., 2006) and 2 ppm Pb (R124, Reunion island glass) are represented at
990 top-left to indicate the external reproducibility. Melt inclusions plot generally in the vicinity
991 of their whole rock, extending in some cases (ACO95-62 and ACO95-56) the range of Pb
992 isotope compositions of the lava, indicating that some melt inclusions appear to show
993 heterogeneity of parental magmas.

994
995 Fig. 5: Insert: at a given $^{206}\text{Pb}/^{204}\text{Pb}$, São Miguel whole rocks (red open circles in the pink
996 area) have higher $^{208}\text{Pb}/^{204}\text{Pb}$ than Central Group rocks (shaded grey area). São Miguel melt
997 inclusions were chosen from whole rocks that best represent the extreme composition of the
998 “Nordeste component”. Main figure: $^{207}\text{Pb}/^{206}\text{Pb}$ versus $^{208}\text{Pb}/^{206}\text{Pb}$, with São Miguel melt
999 inclusions (filled red circles, this study) compared to melt inclusions, glasses, and whole
1000 rocks from islands representing different mantle endmembers. Data represented here are not
1001 extensive (filtered for $\text{SiO}_2 < 53$ wt. %) and do not represent all the published data. Melt
1002 inclusions are filled symbols, and open symbols are whole rocks or glasses. Symbol shapes
1003 are specific to each locality. Data sources are: São Miguel whole rocks (Davies et al., 1989;
1004 Turner et al., 1997; Widom et al., 1997; Moreira et al., 1999; Elliott et al., 2007; Beier et al.,

1005 2007); Mangaia (HIMU) melt inclusions (Cabral et al., 2014); Pitcairn (EMI) glasses
1006 (Woodhead and Devey, 1993); MAR whole rocks and glasses (Agranier et al., 2005; Kelley
1007 et al., 2013); Samoa (EMII) glasses (Workman et al., 2006); and Tahaa (EMII) melt
1008 inclusions (Saal et al., 2005). Whole rock and melt inclusions of São Miguel mainly overlap.
1009 The 2σ ellipsoid errors for repeat measurements of standard glasses with 19 ppm (GOR132G
1010 standard; Jochum et al., 2006) and 2 ppm Pb (R124, Reunion island glass) are represented
1011 next to the legend to indicate the external reproducibility.
1012

1013 Fig. 6: Cl concentrations (ppm) as a function of F concentrations (ppm) in São Miguel melt
1014 inclusions (this study) and in Pico island melt inclusions (Métrich et al., 2014). Our data are
1015 compared to measurements of melt inclusions (filled symbols) and glasses (open symbols)
1016 from localities representing different mantle endmembers: Yellowstone melt inclusions
1017 (Stefano et al., 2011), Cook Austral melt inclusions (Lassiter et al., 2002), MORB melt
1018 inclusions (Shaw et al., 2010, Wanless and Shaw, 2012) and glasses (Le Voyer et al., 2015),
1019 Pitcairn glasses (Kendrick et al., 2014), Samoa melt inclusions and glasses (Workman et al.,
1020 2006), and Mangaia melt inclusions (Cabral et al., 2014). Azores melt inclusions are enriched
1021 in F and Cl by a factor of 10 compared to MORB glasses. F and Cl concentrations in melt
1022 inclusions from Azores and Mangaia mainly overlap and are relatively clustered. Azores melt
1023 inclusions are the lowest among OIBs.
1024

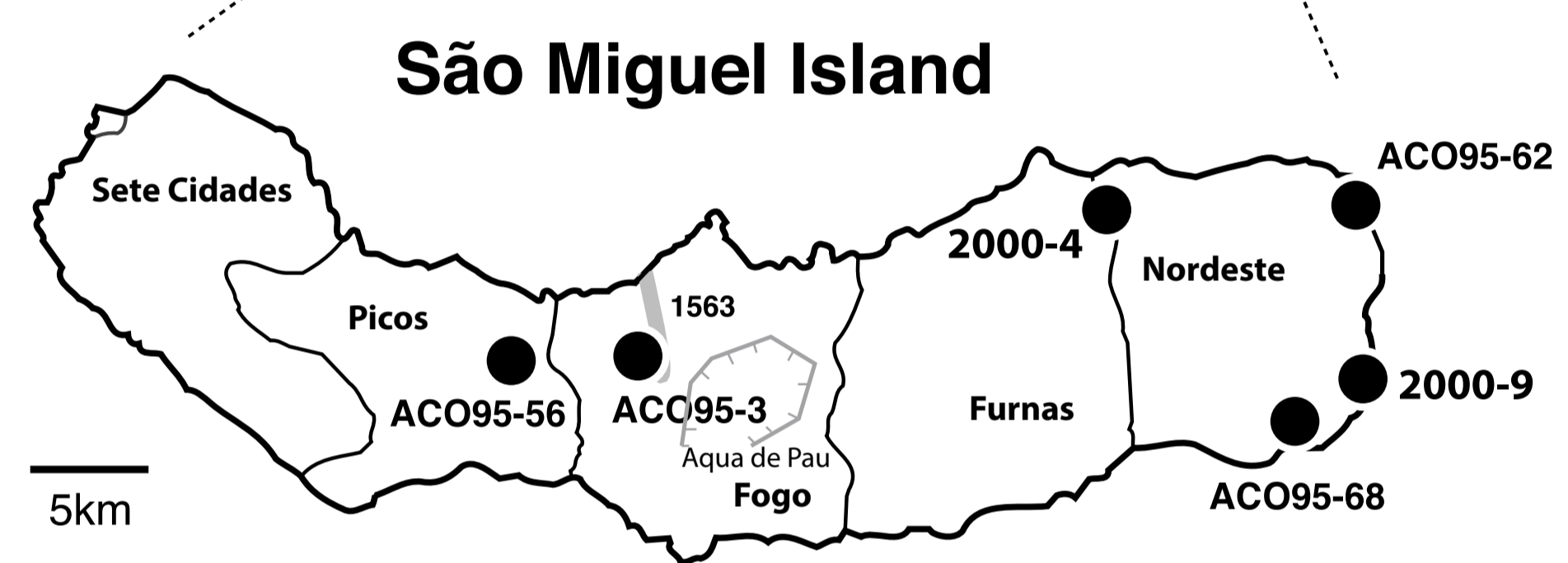
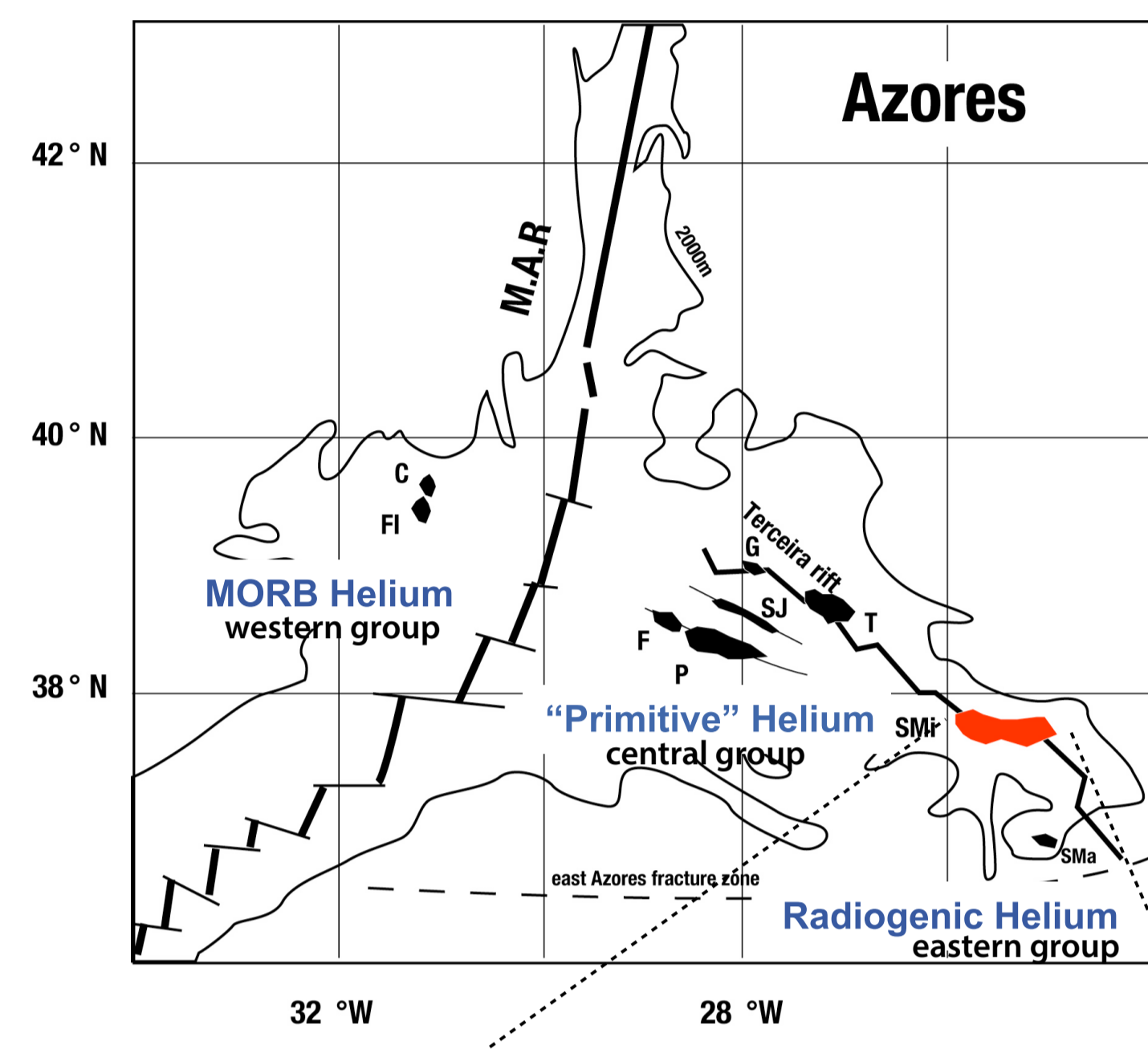
1025 Fig. 7: F/Nd as a function of Cl/K₂O in São Miguel melt inclusions and other mantle
1026 endmember localities (symbols and references as in Fig. 7). Tuvalu glass data (brown open
1027 diamonds) are also plotted since they might represent “real HIMU” volatile element
1028 compositions (Jackson et al., 2015). MORB and Samoan data that were suspected of
1029 assimilation of seawater contaminated material are represented by smaller, lighter symbols
1030 when Cl/K₂O > 0.05 (Michael and Cornell, 1998). The Cl/K₂O > 0.05 ‘cut-off’ discards much
1031 of the Cook Austral data (Lassiter et al., 2002) since they suffered from assimilation of
1032 seawater related components. There is a positive correlation (outlined by the shaded gray
1033 area) between F/Nd and Cl/K₂O from melt inclusions or glasses from OIBs representing
1034 mantle endmembers (Samoa EMII, Pitcairn EMI, Mangaia HIMU), and Azores melt
1035 inclusions from Pico (Métrich et al., 2014) and São Miguel (this study) plot along this
1036 correlation. The relatively tight domain of variation for São Miguel melt inclusions allows us
1037 to propose characteristic values of Cl/K₂O (0.035 ± 0.011) and F/Nd (23.1 ± 3.4) for the São
1038 Miguel parental magma.
1039

1040 Fig. 8: ²⁰⁷Pb/²⁰⁶Pb (red filled circles, red scale at left) and FeO concentrations (blue crosses,
1041 blue scale at right) plotted against S concentrations in ppm for São Miguel melt inclusions.
1042 São Miguel melt inclusions are at sulfide saturation, which explains the relationship between
1043 S and FeO (the solubility of S increases with increasing FeO content at sulfide saturation; e.g.
1044 Li and Naldrett, 1993; O’Neill and Mavrogenes, 2002). Curves represent model results of
1045 mixing between sulfide and basaltic melts for two contrasting Kd^{Pb} values (following Hart
1046 and Gaetani, 2016) of 140 (top curve) and 30 (bottom curve). The best fit to our data is
1047 represented by the center curve (Kd^{Pb} = 70). The sulfide melt is a FeS melt (S = 360000 ppm;
1048 ²⁰⁷Pb/²⁰⁶Pb = 0.857) and the basaltic melt corresponds to Pb = 2 ppm and ²⁰⁷Pb/²⁰⁶Pb = 0.780,
1049 with S = 500 ppm (the lowest S concentrations measured in our melt inclusions). Tick marks
1050 along the curves are 0.06% increments of the sulfide melt mixing proportion. Less than 0.4%
1051 of sulfide is needed to account for the positive correlation of Pb-isotopes and S contents
1052 observed in our melt inclusions. Pb concentration in the sulfide must be high, between 60 and
1053 280 ppm, indicating the sulfide is of shallow origin (Hart and Gaetani, 2016).
1054

1055 Fig. 9: S concentration measured in São Miguel melt inclusions as a function of Sulfur
1056 Concentration at Sulfide Saturation. SCSS is calculated following Fortin et al. (2015). For
1057 melt inclusions not analysed for H₂O content, we assumed H₂O=1552 ppm, the maximum
1058 measured H₂O of this study; this value most likely represents a minimum value because they
1059 melt inclusions are already partly degassed (see section 5.2.1 for details). Temperature was
1060 set at 1200°C (homogenization temperature) and we conservatively chose the pressure value
1061 to be 0.012 MPa, the lowest given by our São Miguel melt inclusions (MagmaSat
1062 calculation). Using our maximum pressure value slightly shifts points to the left, but the two
1063 undersaturated melt inclusions remain undersaturated. Error bars represent 20% relative
1064 uncertainty on the sulfur measurements. The area between the thin dotted lines is the
1065 uncertainty band representing a variation of ±50% around an ideal value (see Fig. 6b of
1066 Fortin et al., 2015; assessed by the relative difference between modelled S and measured S
1067 concentrations for natural samples with less than 2000 ppm S). All São Miguel melt
1068 inclusions are at S saturation (red filled symbols) except for two S-undersaturated melt
1069 inclusions (ACO95-62i, its replicate, and 9-4-00; 3 white circles). One representative Pico
1070 melt inclusion (yellow filled circle) is reported for comparison; it is also at S saturation.
1071

1072 Fig. 10: F/Nd as a function of ²⁰⁷Pb/²⁰⁶Pb for São Miguel melt inclusions and mantle
1073 endmembers HIMU, EMI, EMII, and DMM. References and symbols are as in Figure 7; E-
1074 MORB glass/melt inclusion data are from Gale et al., 2013; Shimizu et al., 2016. The glasses
1075 and melt inclusions from the mantle endmembers define a negative trend between F/Nd and
1076 ²⁰⁷Pb/²⁰⁶Pb, and São Miguel melt inclusions fall on this correlation. F/Nd is therefore a
1077 reliable tracer of source when comparing OIBs. F/Nd of São Miguel melt inclusions
1078 (23.1±3.4) is similar within error to the value of the canonical ratio 21±4 (Workman et al.,
1079 2006).
1080

1081



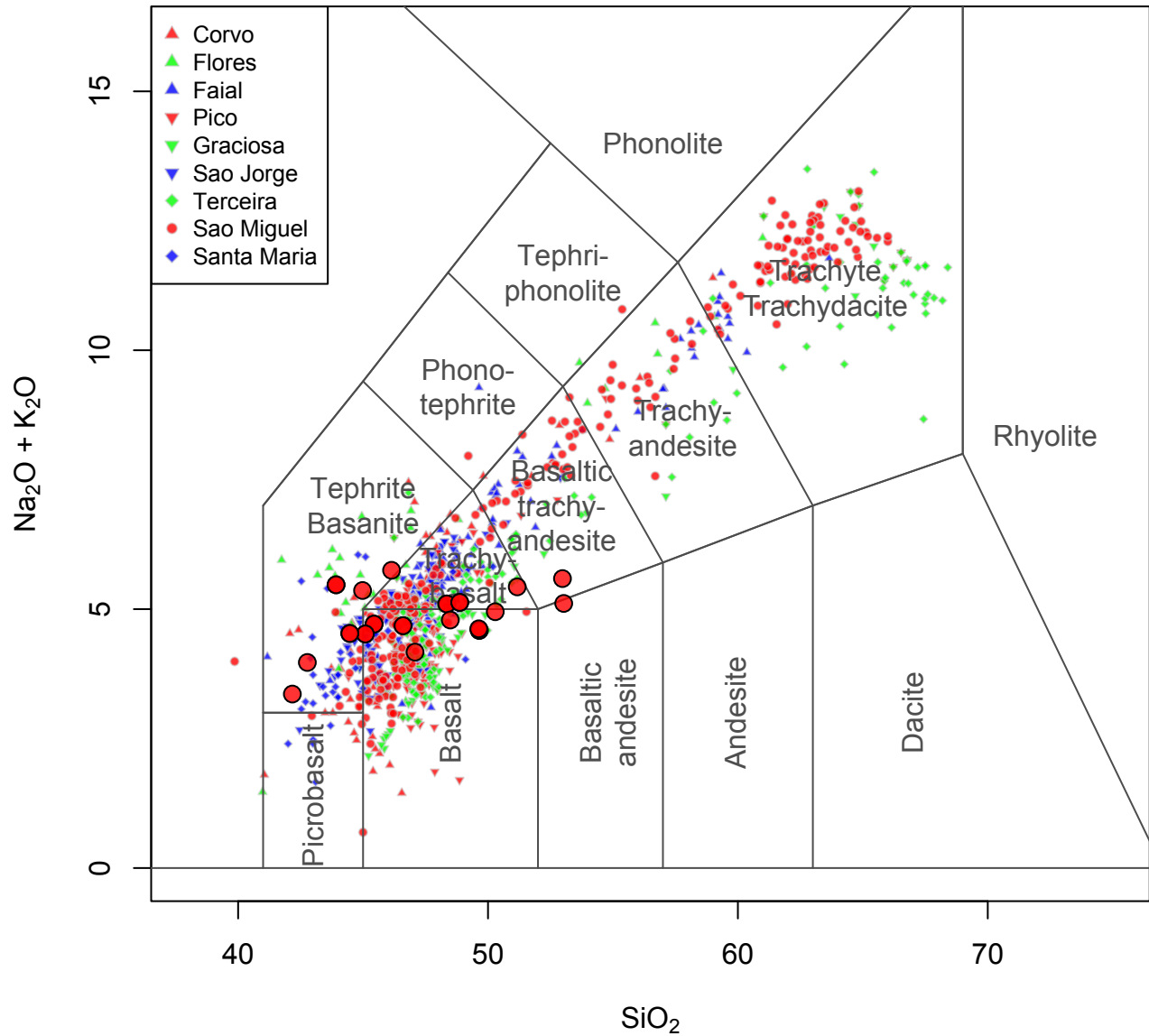


Figure 3a

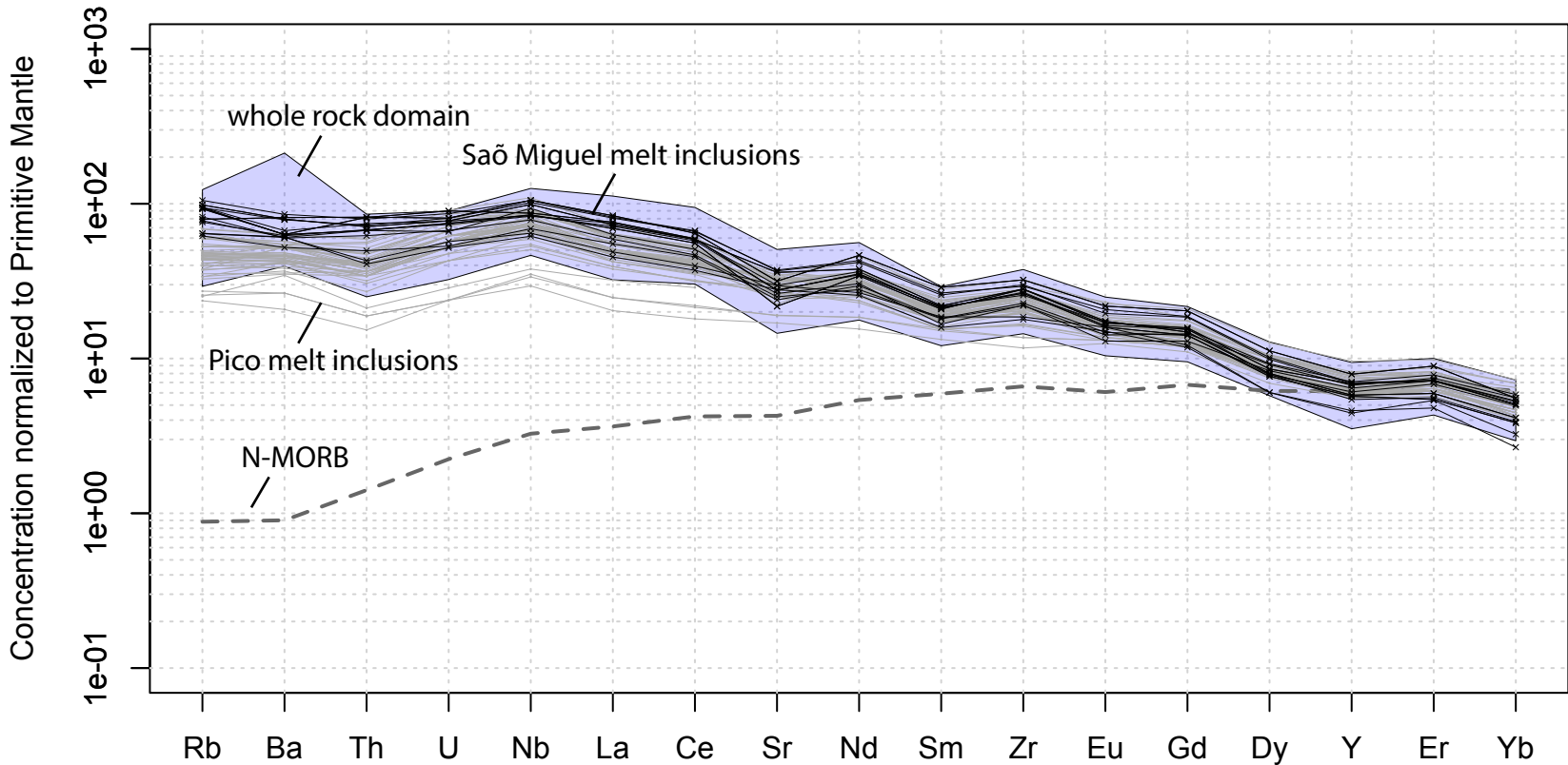
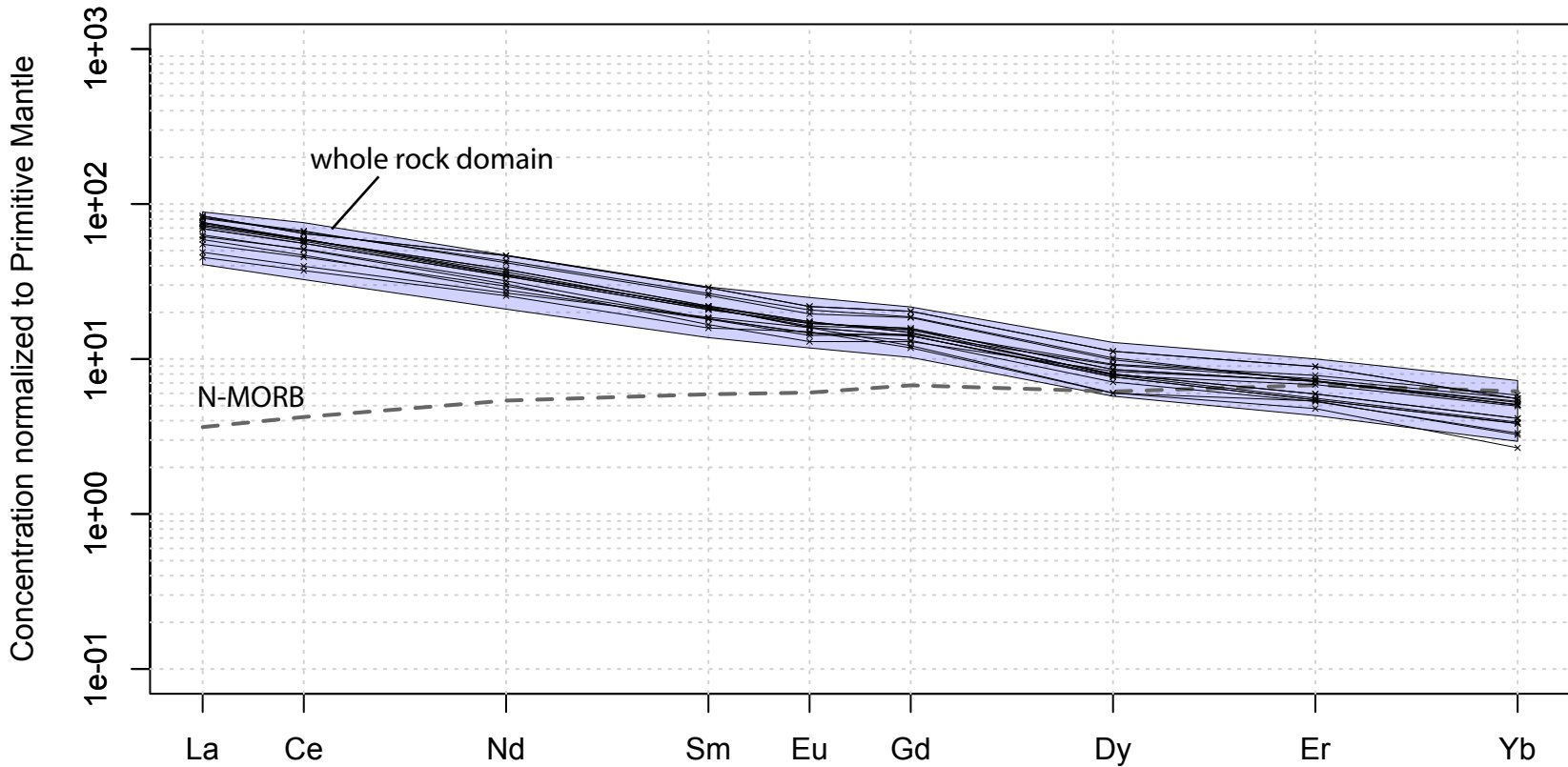


Figure 3b



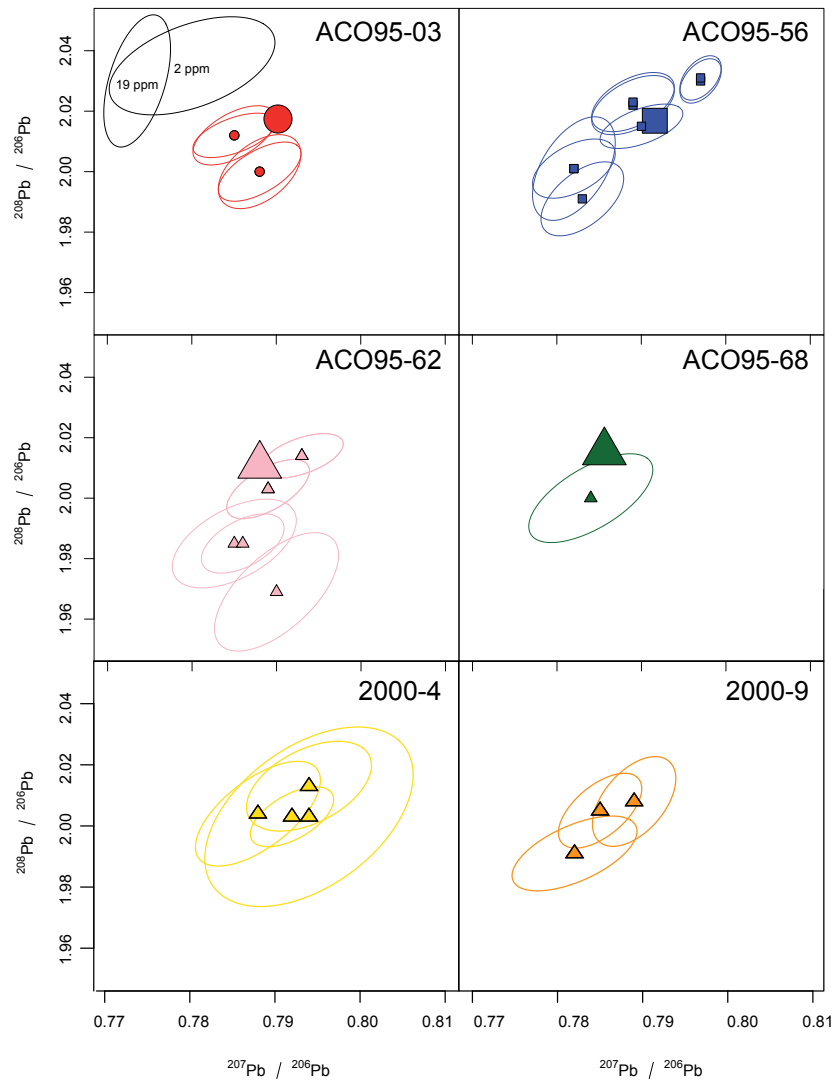


Figure 5

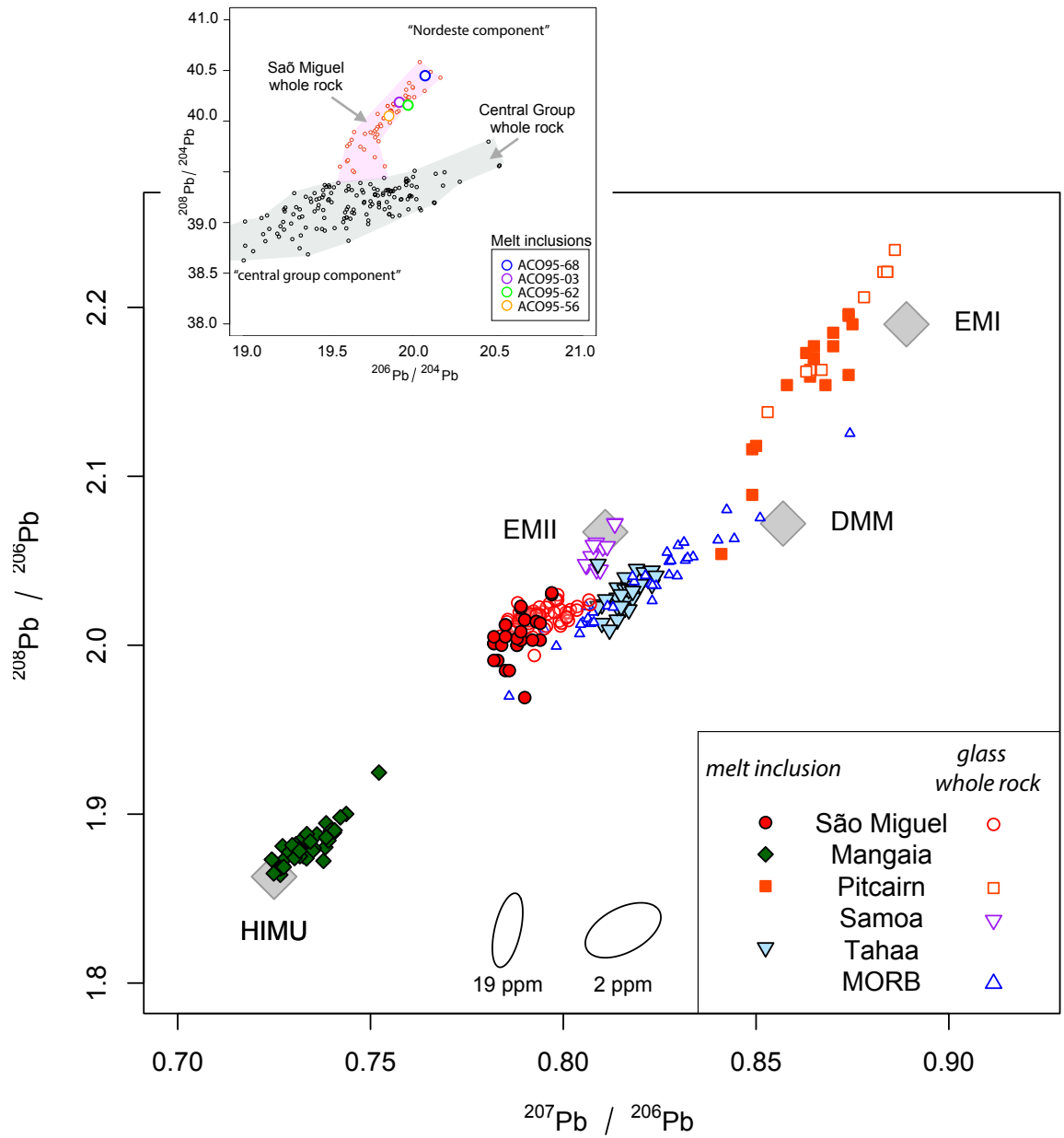


Figure6

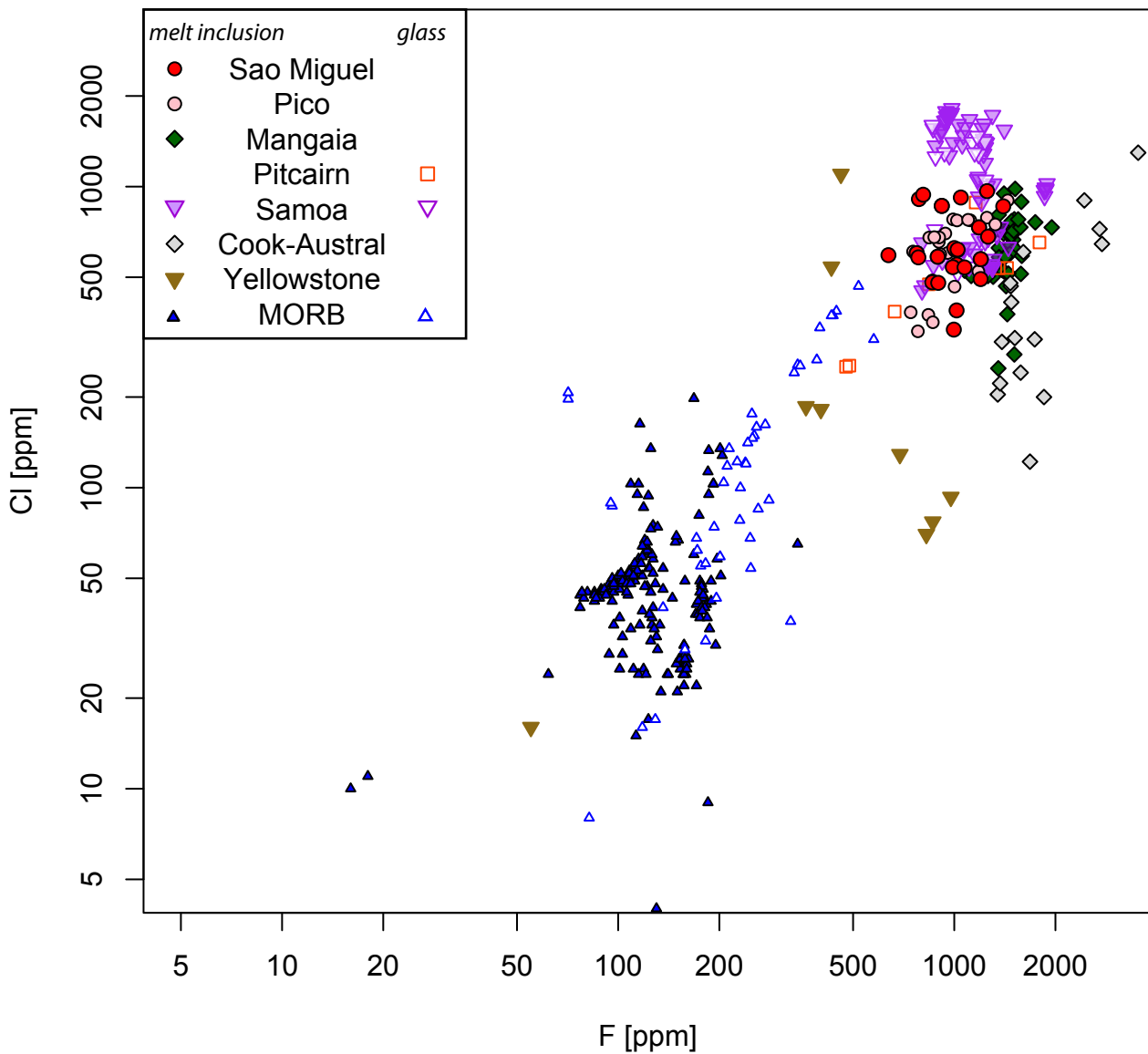
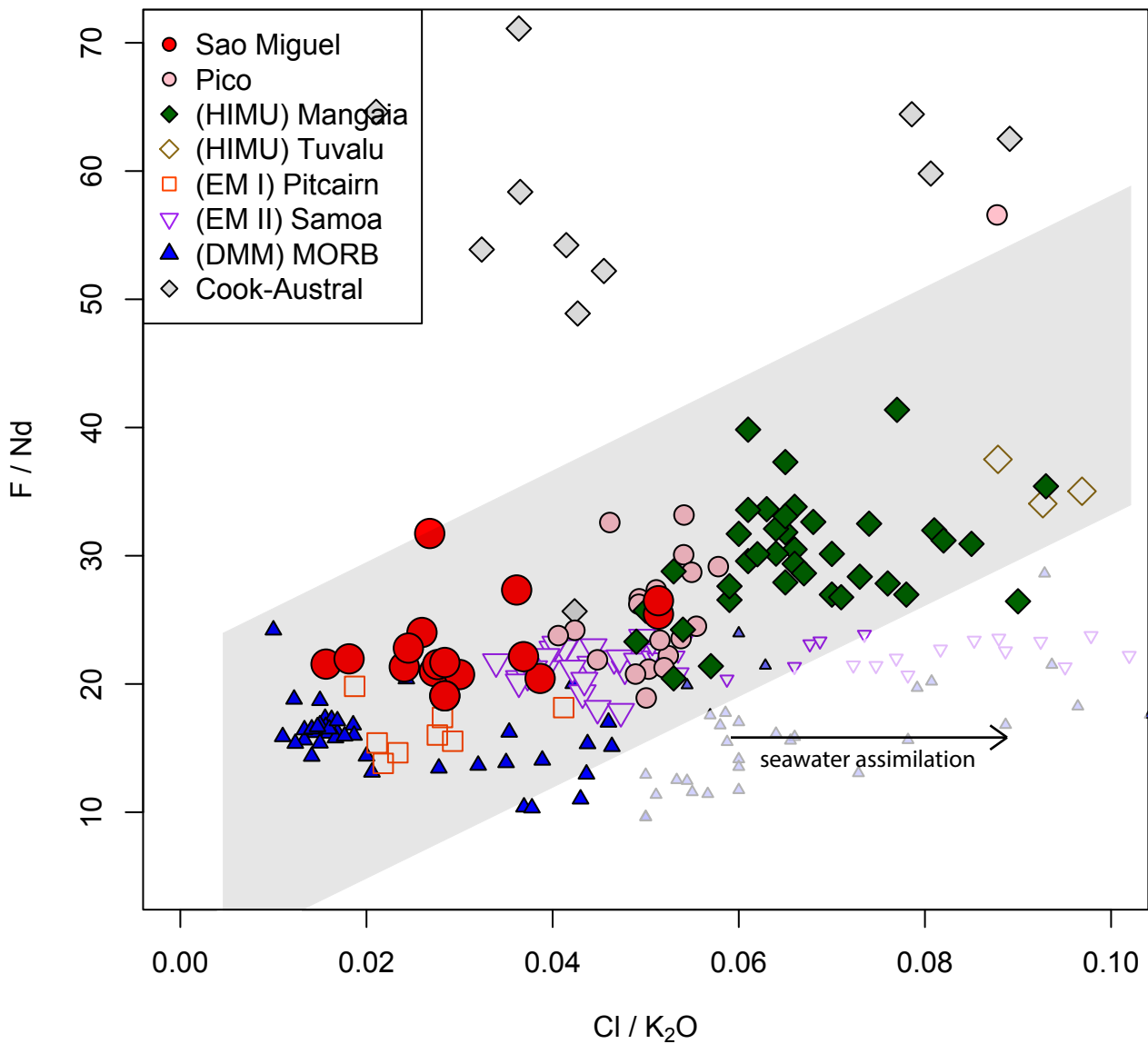


Figure 7



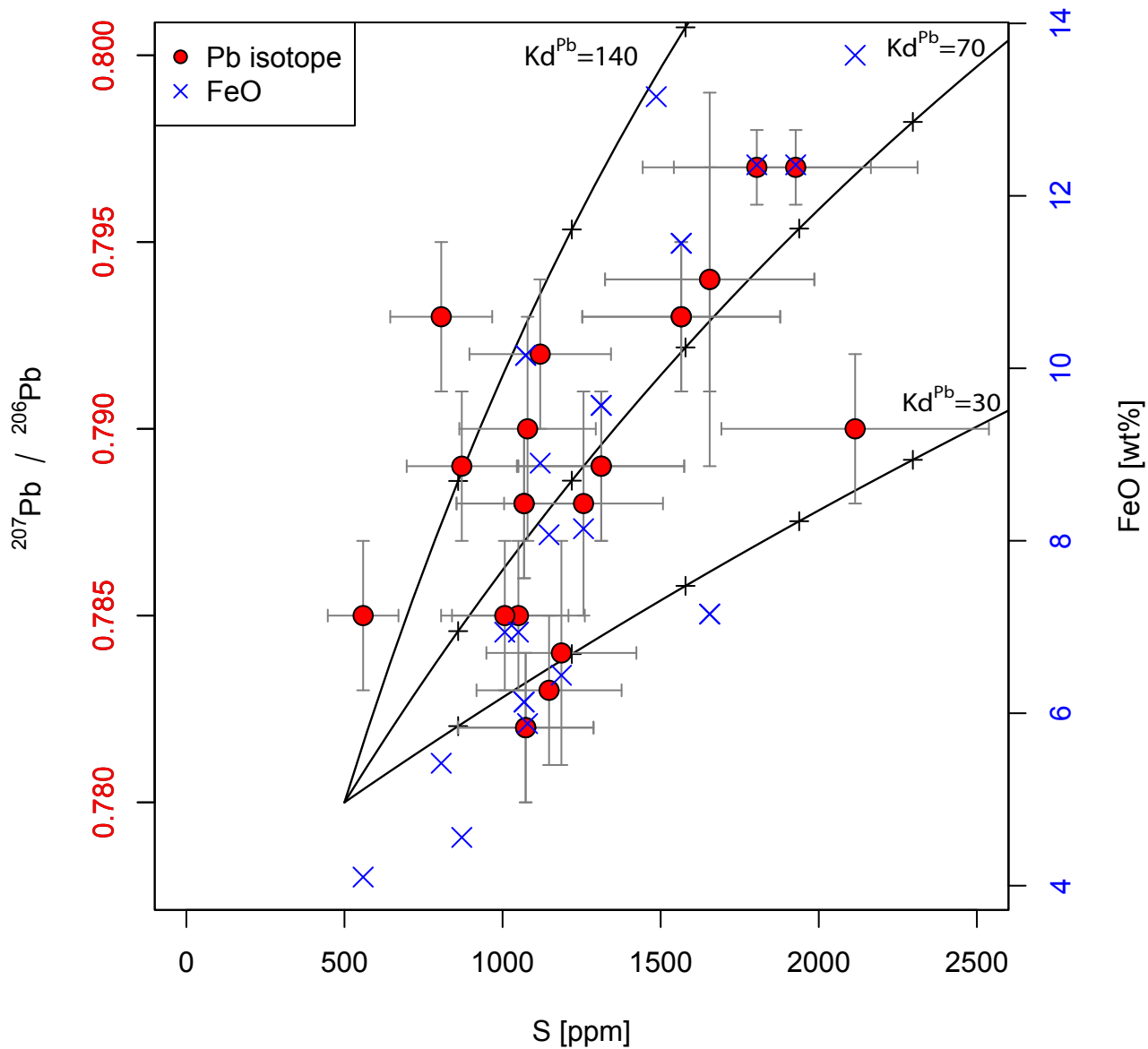


Figure9

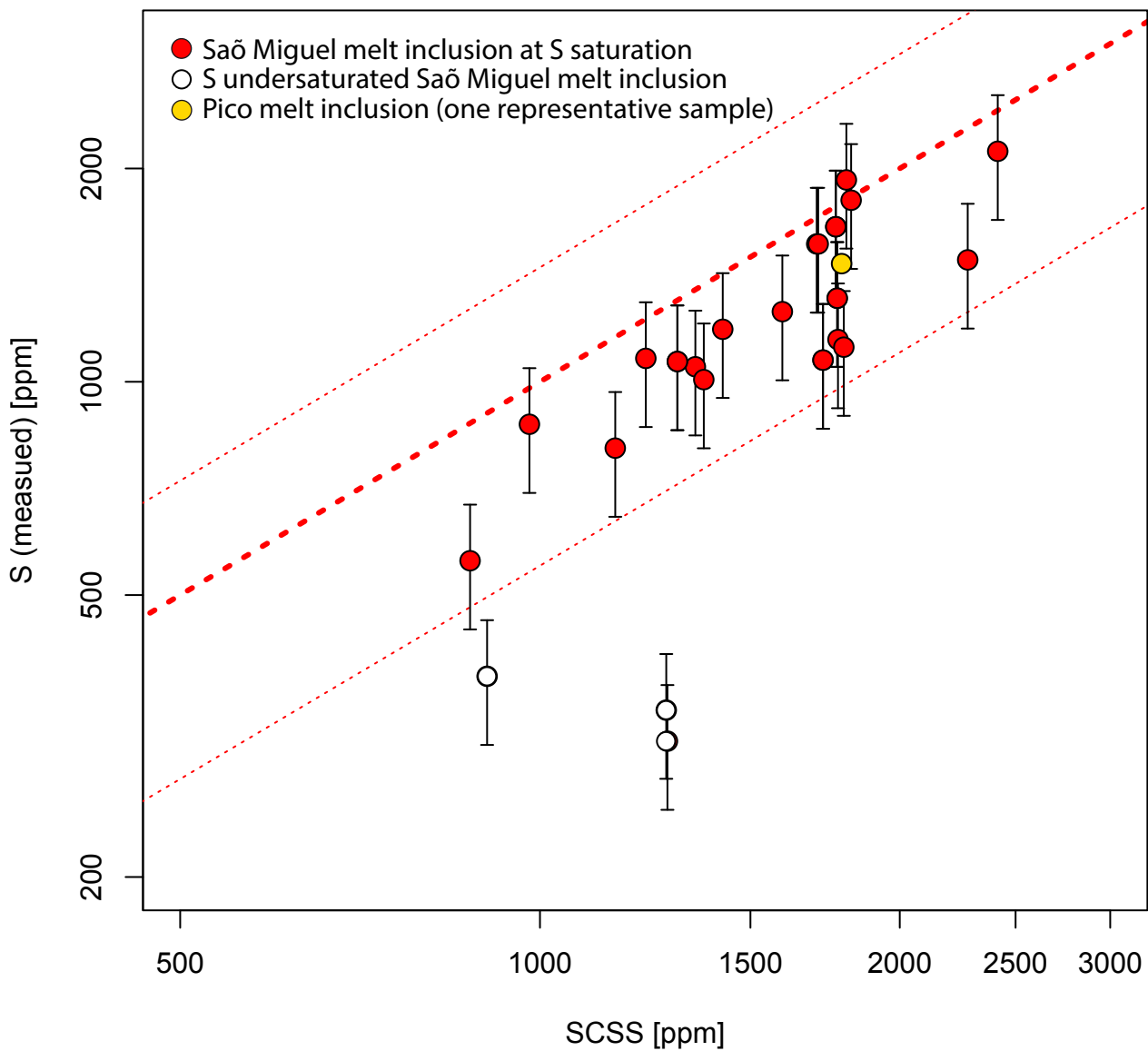
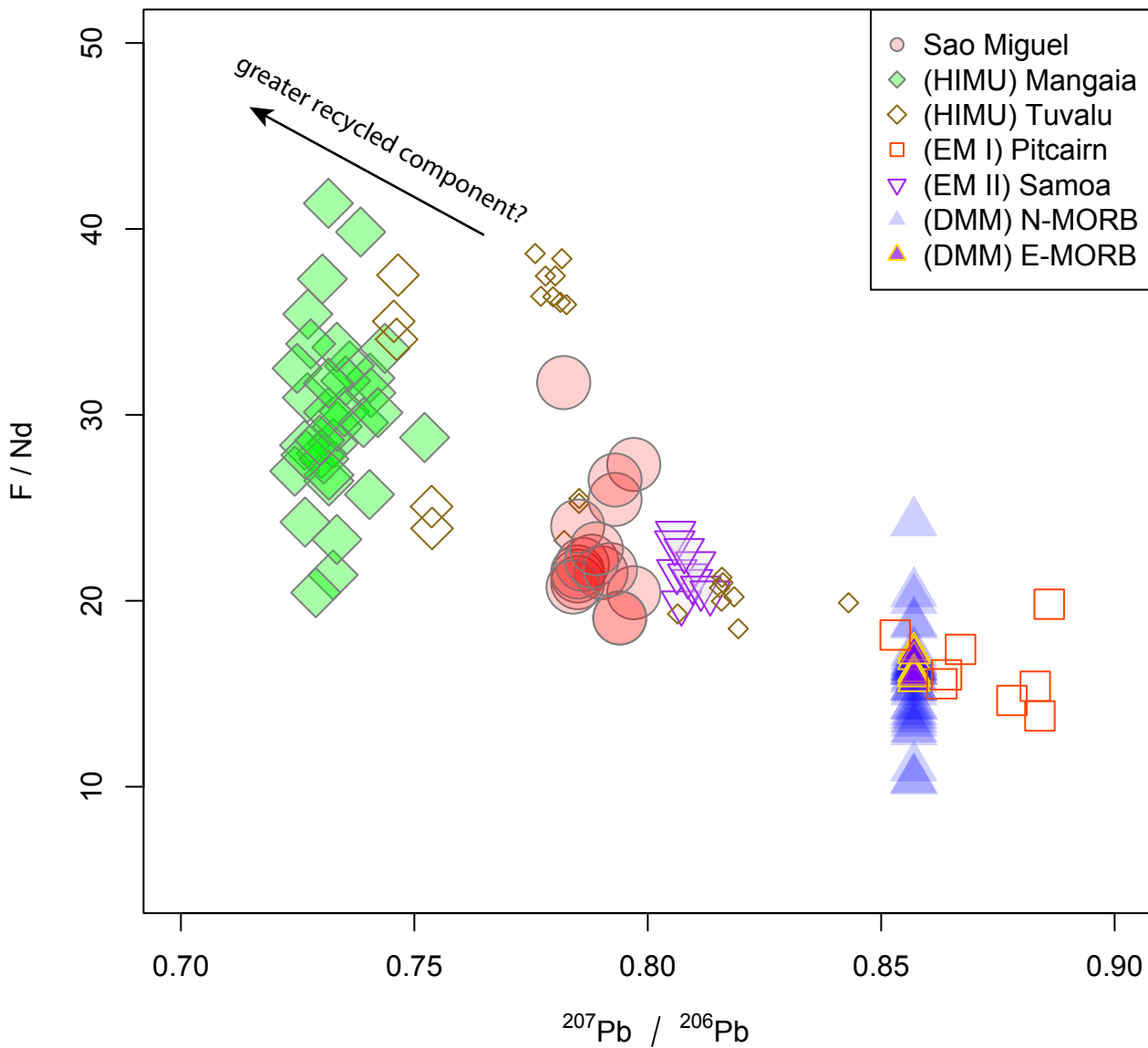


Figure 10



ACO95-03	n.d.	n.d.	n.d.	0.79017	2.01741	19.9197	15.7398	40.1871
ACO95-56	n.d.	n.d.	n.d.	0.79158	2.01683	19.8583	15.7197	40.0516
ACO95-62	n.d.	n.d.	n.d.	0.78801	2.01078	19.9709	15.7376	40.1577
ACO95-68	n.d.	n.d.	n.d.	0.78561	2.01521	20.0716	15.7686	40.4488
NBS 981	n.d.	n.d.	n.d.	0.91459	2.16707	16.9356	15.4891	36.7006

Errors on the volatile element measurements represent 1 sigma error in ppm. Errors for Pb-isotope measurements in melt inclusions represent 1 standard error of the mean.

For whole rock Pb-isotope analysis an external precision inferred by repeated analysis of NBS 980 standard gives a relative 2σ error of 40, 60, 150, 160 and 170 ppm for $^{207}\text{Pb}/^{206}\text{Pb}$, $^{208}\text{Pb}/^{206}\text{Pb}$, $^{206}\text{Pb}/^{204}\text{Pb}$, $^{207}\text{Pb}/^{204}\text{Pb}$ and $^{208}\text{Pb}/^{204}\text{Pb}$, respectively (Vlastélic et al., 2009). When H_2O and CO_2 measurements are reported, the entire volatile suite (H_2O , CO_2 , F, S, Cl) were done by SIMS (11 MI out of 19), and [#]the pressure of saturation $\text{H}_2\text{O}-\text{CO}_2$ was estimated using model Magmat Sat (Ghiorso, 2015). When “only” F, Cl and S are reported, the analysis were done by EMP. * signs the presence of a bubble in the melt inclusions.

For the plots with Pb isotopes and volatiles (Fig. 8 and 9), every “melt inclusion duplicate” was assigned the volatile values of its “parent-melt inclusion”.

Table2

[Click here to download Table: Table 2.pdf](#)Table 2: Major elements corrected compositions* of 19 homogenized olivine-hosted melt inclusions from Sao Miguel, Azores (in wt%) and size of the melt inclusions (long axis (L) and short axis (l), in μm).

	Na ₂ O	MgO	SiO ₂	Al ₂ O ₃	K ₂ O	FeO _{tot}	MnO	CaO	TiO ₂	P ₂ O ₅	Kd	Mg#	Size L x l (μm)	
ACO95-03a	2.81	7.11	48.35	14.11	2.29	6.94	0.10	13.53	4.13	0.62	0.27	87.1	107	37
ACO95-03b	3.05	5.54	49.65	15.51	1.54	6.13	0.08	13.97	3.94	0.56	0.28	85.4		
ACO95-56a	1.98	16.08	42.17	11.44	1.38	13.63	0.20	8.92	3.68	0.52	0.27	88.7		
ACO95-56c	2.55	9.94	47.08	11.60	1.62	8.07	0.04	14.69	3.89	0.52	0.28	88.7		
ACO95-56e	2.64	10.12	46.60	12.32	2.04	9.57	0.14	12.31	3.62	0.65	0.27	87.5		
ACO95-56f	3.09	6.35	43.92	16.25	2.38	12.36	0.22	9.89	4.73	0.82	0.28	76.9	72.8	63.5
ACO95-56g	2.88	10.29	45.44	14.45	1.83	10.15	0.16	10.08	4.14	0.58	0.28	86.7		
ACO95-62b	2.88	4.92	50.29	15.95	2.07	5.42	0.18	13.78	3.98	0.53	0.28	85.2		
ACO95-62c	2.39	8.34	42.77	14.60	1.58	13.15	0.26	11.43	4.84	0.63	0.28	80.0		
ACO95-62d	2.84	6.94	45.09	15.80	1.68	11.45	0.07	11.65	3.94	0.54	0.28	85.4	95.6	85.2
ACO95-62h	2.88	5.67	49.63	15.61	1.74	5.88	0.08	14.11	3.90	0.50	0.28	86.1	96.2	93.2
ACO95-62i	2.99	6.01	48.87	15.85	2.14	6.33	0.03	12.47	4.41	0.91	0.28	86.1	83.1	74.1
ACO95-68a	2.73	7.91	48.49	13.13	2.06	6.44	0.10	14.34	4.15	0.66	0.28	88.8		
2000-4-2	2.51	4.46	44.47	15.55	2.02	7.15	0.13	15.95	7.10	0.66	0.27	80.4		
2000-4-4	3.13	6.04	46.14	14.60	2.62	8.14	0.08	13.19	5.32	0.73	0.27	83.1		
2000-4-5	2.96	5.48	44.98	14.56	2.40	8.90	0.15	13.93	5.89	0.78	0.27	80.4		
2000-9-1	3.03	3.42	53.03	17.32	2.08	4.10	0.04	12.65	3.84	0.49	0.28	83.9		
2000-9-2	3.23	3.36	51.17	17.52	2.20	4.56	0.11	12.88	4.30	0.69	0.28	82.2		
2000-9-4	3.75	3.17	52.98	18.31	1.84	4.29	0.15	11.53	3.31	0.68	0.28	82.6		

* Reported values are corrected for olivine post-entrapment crystallization, and normalized to 100% on a volatile-free basis. Uncertainty is not assessed since the accuracy is olivine correction model dependent. Precision is proportionally equal to electron microprobe measurements (see electronic annex.)

Table3

[Click here to download Table: Table 3.pdf](#)Table 3: Trace elements corrected compositions* (in $\mu\text{g.g}^{-1}$) of homogenized 12 olivine-hosted melt inclusions from Sao Miguel, Azores.

	Rb	Sr	Y	Zr	Nb	Ba	La	Ce	Nd	Sm	Eu	Gd	Dy	Er	Yb	Hf	Ta	Th	U
ACO95-03a	58.8	582	25.9	296	62	442	52.2	106	48	9.5	2.7	7.7	5.6	2.38	1.89	7.10	3.64	6.94	1.89
ACO95-56f	62.4	760	26.4	315	70	556	50.2	104	51	9.7	2.9	8.1	5.9	2.61	2.04	7.79	4.16	6.04	1.63
ACO95-62d	40.7	624	20.9	208	46	424	33.5	70	36	8.3	2.7	6.6	4.4	2.10	1.32	4.93	2.52	3.65	1.20
ACO95-62h	39.3	505	27.7	255	49	365	37.8	81	40	8.1	2.5	7.7	5.8	2.99	2.45	6.73	2.78	4.22	1.12
ACO95-62i	59.7	459	31.2	314	60	442	47.6	99	46	9.3	2.8	8.6	6.3	3.14	2.50	7.69	3.57	5.72	1.57
ACO95-68a	48.3	627	24.7	300	59	434	51.4	104	49	9.4	2.7	8.4	5.8	2.45	1.93	7.45	3.60	5.78	1.54
2000-4-2	50.4	667	36.0	361	75	569	57.5	114	63	12.8	3.7	11.1	8.3	3.91	2.73	9.91	4.77	6.96	1.70
2000-4-4	66.8	777	31.3	335	75	597	56.2	119	57	11.4	3.3	10.1	7.3	3.16	2.59	8.96	4.85	6.77	1.81
2000-4-5	59.8	787	31.7	328	73	550	55.5	117	58	11.8	3.5	10.2	7.5	3.17	2.50	8.56	4.41	6.17	1.69
2000-9-1	49.4	555	29.3	248	67	424	43.4	90	41	7.4	2.2	7.0	6.1	3.15	2.63	6.39	4.16	5.71	1.39
2000-9-2	60.3	585	32.2	287	60	468	49.1	102	47	9.6	2.9	8.3	6.8	3.43	2.88	7.70	3.68	6.33	1.62
2000-9-4	52.2	528	30.5	246	56	420	40.5	83	38	8.0	2.4	7.9	6.7	3.26	2.74	6.23	3.36	5.29	1.41

* Reported values are corrected for olivine post-entrapment crystallization, and normalized to 100% on a volatile-free basis. Relative 1σ standard errors are better than 3% for Rb, Sr, Y, Zr, Nb, Ba, La, Ce, less than 4% for Nd, better 9% for Sm, Eu, Gd, Dy, Er, Hf, Ta, Th and U, and 12% for Yb. Measurements of samples that are not presented here were attempted, but failed due to the lack of inclusion volume.

Table 1A: Major elements compositions of 19 olivines from Sao Miguel, Azores (in wt%).

	MgO	SiO2	Al2O3	FeO	Mno	CaO
ACO95-03a	45.95	41.11	0.03	12.15	0.17	0.29
ACO95-03b	45.92	39.68	0.03	13.94	0.20	0.26
ACO95-56a	47.20	40.16	0.04	10.69	0.15	0.30
ACO95-56c	48.08	39.87	0.04	10.89	0.13	0.29
ACO95-56e	47.63	40.08	0.02	12.08	0.21	0.28
ACO95-56f	39.28	38.28	0.04	21.01	0.27	0.21
ACO95-56g	46.37	39.70	0.05	12.67	0.17	0.28
ACO95-62b	44.99	40.00	0.04	13.94	0.18	0.30
ACO95-62c	40.91	38.75	0.04	18.24	0.24	0.24
ACO95-62d	45.08	39.55	0.05	13.76	0.21	0.28
ACO95-62h	46.34	39.90	0.03	13.35	0.19	0.28
ACO95-62i	46.34	39.90	0.03	13.35	0.19	0.28
ACO95-68a	48.35	39.26	0.05	10.89	0.16	0.25
4/2/2000	41.79	39.15	0.00	18.20	0.29	0.36
4/4/2000	43.68	39.64	0.02	15.80	0.34	0.34
4/5/2000	41.99	39.81	0.00	18.26	0.23	0.54
9/1/2000	44.01	40.03	0.00	15.08	0.20	0.31
9/2/2000	42.72	39.47	0.00	16.53	0.17	0.28
9/4/2000	43.73	40.45	0.00	16.37	0.15	0.27

Table 1B: Major elements uncorrected compositions of 19 homogenized olivine-hosted melt inclu

	Na2O	MgO	SiO2	Al2O3	K2O	FeO
ACO95-03a	2.58	10.02	47.49	12.96	2.10	7.29
ACO95-03b	2.62	10.72	47.75	13.31	1.33	7.07
ACO95-56a	2.34	9.58	41.83	13.52	1.63	13.98
ACO95-56c	2.38	11.29	45.60	10.83	1.51	7.99
ACO95-56e	2.28	14.45	45.06	10.64	1.76	9.72
ACO95-56f	2.93	7.42	42.91	15.37	2.25	12.44
ACO95-56g	3.09	7.14	45.37	15.48	1.96	9.81
ACO95-62b	2.50	9.67	48.45	13.85	1.79	6.38
ACO95-62c	2.36	7.94	41.88	14.39	1.56	12.83
ACO95-62d	2.75	7.67	44.53	15.32	1.63	11.38
ACO95-62h	2.50	10.76	48.04	13.53	1.50	6.78
ACO95-62i	2.77	8.62	47.90	14.68	1.98	6.74
ACO95-68a	2.52	10.11	47.06	12.13	1.91	6.58
4/2/2000	2.19	8.73	43.34	13.56	1.76	8.35
4/4/2000	2.94	8.03	45.45	13.71	2.46	8.49
4/5/2000	2.70	8.03	44.00	13.31	2.19	9.45
9/1/2000	2.53	9.89	50.70	14.47	1.73	5.83